LMSC-D057194

UNSTEADY AERODYNAMIC FLOW FIELD ANALYSIS OF THE SPACE SHUTTLE CONFIGURATION

Part I: ORBITER AERODYNAMICS

by

Lars E. Ericsson and J. Peter Reding

April 1976

Prepared Under Contract NAS 8-30652

for

National Aeronautics and Space Administration

(NASA-CR-144332) UNSTEADY AERODYNAMIC FLOW FIELD ANALYSIS OF THE SPACE SHUTTLE CONFIGURATION. PART 1: ORBITER AERODYNAMICS (LOCKHEED MISSILES AND SPACE CO.) 71 P HC $4.50 CSCL 22B G3/18

N76-25328

UNCLAS

42204

Lockheed MISSILES and SPACE COMPANY, INC.

SUNNYVALE, CALIFORNIA

UNSTEADY AERODYNAMIC FLOW FIELD ANALYSIS OF THE SPACE SHUTTLE CONFIGURATION

Part I: ORBITER AERODYNAMICS

by
Lars E. Ericsson and J. Peter Reding

April 1976

Prepared Under Contract NAS 8-30652
for
National Aeronautics and Space Administration

Lockheed Missiles & Space Company, Inc.
A Subsidiary of Lockheed Aircraft Corporation
Sunnyvale, California

ABSTRACT

An analysis of the steady and unsteady aerodynamics of the space shuttle orbiter has been performed. It is shown that slender wing theory can be modified to account for the effect of Mach number and leading edge roundness on both attached and separated flow loads. The orbiter unsteady aerodynamics can be computed by defining two equivalent slender wings, one for attached flow loads and another for the vortex-induced loads. It is found that the orbiter is in the transonic speed region subject to vortex-shock-boundary layer interactions that cause highly nonlinear or discontinuous load changes which can endanger the structural integrity of the orbiter wing and possibly cause snap roll problems. It is presently impossible to simulate these interactions in a wind tunnel test even in the static case. Thus, a well planned combined analytic and experimental approach is needed to solve the problem.

CONTENTS

ILLUSTRATIONS

PRECEDING PAGE BLANK NOT FILMED

ILLUSTRATIONS (Continued)

Figure

Section 1
INTRODUCTION

The aim of the present analysis is to provide the building blocks for a computer program that can predict the aeroelastic characteristics of the space shuttle launch configuration through analytic extrapolation from experimental data, similarly to what was done for the Apollo-Saturn launch vehicle (Refs. 1-3). The most significant difference between the present launch vehicle and the Saturn booster is the presence of a large lifting surface, the orbiter wing. As it is basically a delta wing, analytic means are needed for the prediction of the unsteady delta wing aerodynamics, including the effects of the leading edge vortices. Because of the asymmetric mating of the orbiter to the booster roll-pitch-yaw coupling effects become of concern and it is essential that the yaw-induced rolling moment on the orbiter delta wing can be predicted.

The first step towards the development of this needed analytic capability was taken in References 4, 5 and 6. In the present report this analytic development is taken one step further by including the vortex entrainment effect suggested in Reference 5 and by extending the analysis to account for Mach number effects along the lines discussed in Reference 4. Finally, a critical look is taken at the orbiter wing aeroelastic stability characteristics without the complications introduced by the interference flow field from HO Tank and SRM rockets.

Section 2
DISCUSSION

The analyses in References 4 and 5 will be repeated here to the extent necessary for good readability. The intent is to present the equations in a compressed, unified form such that the design engineer can get all needed information from one source: this report.

2.1 Delta Wing Aerodynamics

In incompressible flow, the normal force on a slender, sharp edged delta wing can be determined as follows (Ref. 7):

$$C_N = K_P \sin\alpha \cos\alpha + K_V \sin^2\alpha \tag{1}$$

K_P and K_V are parameters determining the magnitudes of attached flow and vortex force components respectively. K_V is for all practical purposes a true constant, $K_V \approx \pi$, (Ref. 7); whereas K_P is more or less linearly dependent upon aspect ratio (Fig. 1). Jones slender wing theory (Ref. 8) applies only for $M_\infty = 1$. The deviation between it and potential flow results (Ref. 7) at $M_\infty = 0$ are represented as follows. It is assumed that the area denoted A_{TE} in the inset in Figure 1 carries no load. This accounts in a crude manner for the trailing edge condition at $M_\infty = 0$ (as compared to $M_\infty = 1$). It reduces the delta wing normal force by the factor $\cos^2\theta_{LE}$ giving

$$K_{P1} = \pi(A/2)/\left[1 + (A/4)^2\right] \tag{2}$$

This is the "First Approximation" shown in Fig. 1. The strip loading normal to the leading edge is

$$(1/2)\ (d\ C_{N_\alpha}/d\xi)_L = \left[\pi \sin 2\ \alpha \sin^2\ \theta_{LE}/(b/2\ c_o)\right]\xi \tag{3}$$

It was shown in Reference 5 that the potential flow loading on a delta wing never exceeded 75% of the maximum given by slender wing theory. Applying this "ceiling" changes Eq. (3) to

$$(1/2)\ (d\ C_{Na}/d\xi)_L = \frac{\pi \sin 2\ \alpha \sin^2\ \theta_{LE}}{(b/2c_o)} \times \begin{cases} \xi : \xi \leq 0.7 \\ 0.7 : \xi > 0.7 \end{cases} \tag{4}$$

Integrating Eq. (4) gives

$$\left.\begin{aligned} C_{Na} &= 0.91\ K_{P1} \sin \alpha \cos \alpha \\ C_{ma} &= -(c_o/\bar{c})\ C_{Na}\ (\bar{\xi}_a - \xi_{CG}) \\ \bar{\xi}_a &= 0.64\ (1 - \Delta\xi_{aTE}) \\ \Delta\xi_{aTE} &= \bar{\eta}_a \sin^2\ \theta_{LE} \end{aligned}\right\} \tag{5}$$

$$(\bar{\eta}_a = 4/3\ \pi \text{ for elliptic loading})$$

K_{P1} is given by Eq. (2). The value $0.91\ K_{P1}$ is the "Second Approximation" in Fig. 1 which shows good agreement with potential theory for aspect ratios up to $A = 3$.

It was also shown in Reference 5 that the vortex induced load distribution on a sharp-edged delta wing does not have the triangular shape prescribed by the conic flow assumption used in most theories, but has a "ceiling" similar to that for attached flow. The resulting load distribution for the 70% of the vortex induced loading that is located at the leading edge was shown to be:

$$\frac{1}{0.7}\frac{1}{2}\left(\frac{dC_{NV}}{d\xi}\right)_L = \begin{cases} 1.72\ \pi\ \xi \sin^2\ \alpha: & \xi \leq 0.4 \\ 0.685\ \pi \sin^2\ \alpha: & 0.4 < \xi < 0.9 \\ 6.85\ \pi \sin^2\ \alpha\ (1-\xi): & 0.9 \leq \xi \leq 1.0 \end{cases} \tag{6}$$

and the remaining 30% vortex induced loading produced by the vortex-entrainment effect over the center wing was shown to have the attached flow type distribution given below

$$\frac{1}{0.3}\,\frac{1}{2}\left(\frac{dC_{NV}}{d\xi}\right)_L = \begin{cases} 1.05\,\pi\,\xi \sin^2\alpha : \xi \leq 0.7 \\ 0.735\,\pi \sin^2\alpha : 0.7 < \xi \leq 1.0 \end{cases} \tag{7}$$

Integration of Eqs. (6) and (7) gives:

$$\left.\begin{aligned} C_{NV} &= \pi \sin^2\alpha \\ C_{mV} &= -(c_o/\bar{c})\, C_{NV}\Big[0.7\,(\bar{\xi}_V - \xi_{CG}) \\ &\qquad + 0.3\,(\bar{\xi}_a - \xi_{CG})\Big] \\ \bar{\xi}_V &= 0.56\,(1 - \bar{\eta}_V \sin^2\theta_{LE}) \\ \bar{\xi}_a &= 0.64\,(1 - \bar{\eta}_a \sin^2\theta_{LE}) \end{aligned}\right\} \tag{8}$$

$\bar{\eta}_a = 4/3\,\pi$ and $\bar{\eta}_V$ is given by experimental data (see Fig. 2 and Ref. 9)

It was shown in Reference 5 how the unsteady aerodynamics for the attached flow loads could be determined by using slender wing theory (Ref. 8) on an equivalent delta wing which has been shortened to provide the correct normal force defined by Eq. (5). The effective center chord for this equivalent wing is defined as follows

$$\frac{c_{eff}}{c_o} = 0.955 \cos\theta_{LE}\left[2 - \cos^{-2}\alpha_o\right]^{1/2} \tag{9}$$

Thus, the attached flow unsteady aerodynamics for oscillations in pitch (θ) around ξ_{CG} at $\alpha = \alpha_o$ are given by slender wing theory in the following form

$$\left.\begin{aligned} C_{m_{\theta_a}} &= -\frac{c_o}{\bar{c}}\left(C_{N_\alpha}\right)_{eff.}\cos^2\alpha_o\left[\frac{2}{3}\,\frac{c_{eff.}}{c_o} - \xi_{CG}\right] \\ C_{m_{\dot{\theta}_a}} &= -\left(\frac{c_o}{\bar{c}}\right)^2\left(C_{N_\alpha}\right)_{eff.}\cos\alpha_o\left[\frac{c_{eff.}}{c_o} - \xi_{CG}\right]^2 \\ \left(C_{N_\alpha}\right)_{eff} &= \frac{\pi A}{2}\left(\frac{c_{eff.}}{c_o}\right)^2 \end{aligned}\right\} \tag{10}$$

From Eqs. (9) and (10) the center of pressure is obtained as

$$\frac{2}{3}\,\frac{c_{eff.}}{c_o} = 0.64\left(1 - \frac{1}{2}\sin^2\theta_{LE} + \text{---}\right) \tag{11}$$

whereas Eq. (5) gives

$$\xi_a = 0.64\left(1 - 0.425\sin^2\theta_{LE}\right) \tag{12}$$

That is, the center of pressure is the same for slender wings, $\sin^2\theta_{LE} \ll 1$, as it should be.

Using Lamborne's results (Ref. 10) it was shown in Reference 5 that the vortex induced unsteady aerodynamics could be determined as follows

$$\left.\begin{aligned} C_{m_{\theta_s}} &= -\frac{c_o}{\bar{c}}\,C_{N_{\alpha_V}}\left[0.3\,(\bar{\xi}_a - \xi_{CG}) + 0.7\,(\bar{\xi}_V - \xi_{CG})\right] \\ C_{m_{\dot{\theta}_s}} &= -\left(\frac{c_o}{\bar{c}}\right)^2 C_{N_{\alpha_V}}\Bigg[0.3\sec\alpha_o\left(\frac{c_{eff.}}{c_o} - \xi_{CG}\right)^2 \\ &\qquad - 0.7\,\xi_{CG}\,\frac{U_\infty}{\bar{U}}\,(\bar{\xi}_V - \xi_{CG})\Bigg] \end{aligned}\right\} \tag{13}$$

where $U_\infty/\bar{U} = 0.75$ for oscillations in pitch, and $C_{N\alpha V}$ is given by Eq. (8); $C_{N\alpha V} = \pi \sin 2\,\alpha_o$

Fig. 3 shows the predictions by Eqs. (8) - (13) to agree well with experimental data (Refs. 11 and 12).

2.2 Effect of Leading Edge Roundness

Gersten has shown (Ref. 13) that leading edge roundness has a large effect on delta wing aerodynamics (Fig. 4). A large part of the measured decrease in lift and pitching moment is probably due to the delay of leading edge separation caused by leading edge roundness. The 12.5% truncation of the wing tip (see sketch in Fig. 4) would not have any effect on the delta wing lift and moment according to the present analytic model (see inset in Fig. 1). Recent results by LaMar (Ref. 14) also indicate that the effect would be negligibly small.

According to Ville (Ref. 15), leading edge separation should, in two-dimensional flow, occur at an angle of attack of $\alpha_{2Ds} = f\left(\frac{r_N}{c}, Re\right)$. It is clear that the three-dimensional flow will delay the separation in the cross flow plane to an angle of attack $\alpha_{Ns} > \alpha_{2Ds}$. An estimate of this delay can be made by defining an effective aspect ratio $A_N = 4\,c_o/b$ for half* the delta wing in the cross flow plane. It can be assumed that C_{Lmax} is relatively independent of aspect ratio, (Refs. 16 and 17). Thus, one obtains

$$\alpha_{Ns} = \alpha_{2Ds}\,(1 + \tan\,\theta_{LE}) \tag{14}$$

For the small angles of attack of interest the angle of attack α_s is simply

$$\alpha_s = \alpha_{2Ds}\,(1 + \tan\,\theta_{LE})\,\sin\,\theta_{LE} \tag{15}$$

*The leading edge flow is insensitive to what happens on the other wing half.

Experimental results (Ref. 18) indicate that leading edge stall on the NACA-0012 airfoil will occur in the angle of attack range $12.5° \leq \alpha_{2Ds} \leq 18°$ depending upon the Reynolds number. For the orbiter main wing $\Lambda = 45°$, which in Eq. (15) gives $\alpha_s = \alpha_{2Ds} \sqrt{2}$. Thus, for $M_\infty = 0$ one obtains $17.7° \leq \alpha_s \leq 25.5°$.

The Mach number M_N normal to the leading edge is simply

$$M_N = M_\infty \cos\alpha \left[\tan^2\alpha + \sin^2\theta_{LE}\right]^{1/2} \tag{16}$$

Using the two-dimensional data for the separated flow boundaries of the NACA 64A 012 airfoil (See Ref. 19 and Fig. 5a) as a guide line, the prediction for $M_\infty = 0$ can be extended to transonic speeds as is shown in Figure 5b. The bars in Figure 5b represent oil flow data for the orbiter (Ref. 20). As the pictures were only taken at every 5 degrees of angle of attack, the bars span over $\Delta\alpha = 5°$, with the bottom indicating attached leading edge flow and the top of the bar established leading edge separation. Considering all the complications due to three-dimensional flow effects, which will be discussed later in this report and in more detail in Part II (Ref. 21), the agreement is rather good between predicted and measured separated flow boundaries. It should be noted that without the aspect ratio correction, Eq. (14), the predicted α_s-values would be exactly half of what is shown in Figure 5b. For this reason the predicted boundary in Figure 18 of Ref. 22 is much too low.

For the test data in Figure 4 a value of $\alpha_{2Ds} = 13°$ is suggested giving $\alpha_s = 3.95°$. Substituting α with $(\alpha - \alpha_s)$ in Eqs. (5) and (8) gives the rounded leading edge effect shown by the difference between the dashed and solid line curves in Figure 4. Although the predicted effect of leading edge roundness is in the right direction, it is less than what was observed experimentally. One possible reason for this is the following: It was discussed in Reference 5 how a slackening of the vortex-induced load buildup was observed to occur aft of 40% center chord ($\xi > 0.4$). This was attributed to a "loosening" of the vortex shedding; i.e., the vortex becomes less concentrated. Such an increase of the vortex core could occur for two possible reasons: 1) the center core axial velocity is decreasing or 2) the vortex shedding mechanism from the leading edge has changed. If the second reason is the significant one, the leading edge roundness could be expected to contribute to further "loosening" of the vortex shedding with associated loss in vortex-induced lift. However, if the first reason dominates, which would be in accordance with the causative mechanism for the more severe "loosening" phenomenon called vortex burst (Refs. 23 – 25), the leading edge roundness effect should be accounted for by the ($\alpha - \alpha_s$) correction. This appears to be the case judging by the good agreement between predictions and experimental dynamic results[#] (Ref. 11) for a delta wing with rounded leading edge (Fig. 6).

That this purely static effect of leading edge roundness suffices to explain the dynamic effects is somewhat surprising in view of the large overshoot of static stall observed in dynamic testing of airfoils (Ref. 26). However, it is in agreement with the dominance of three-dimensional flow observed by Lambourne (Ref. 10). He showed that it is the flow conditions at the apex at an earlier time instant that determine the instantaneous downstream vortex strength.

2.3 Lateral Characteristics

The dominant lateral characteristic of a sideslipping delta wing is the rolling moment derivative $C_{\ell\beta}$ (Fig. 7). At an angle of sideslip, the effective apex angle of the windward side is increased by an amount $\Delta\theta_{LE}$ (see Fig. 8).

$$\Delta\theta_{LE} = \tan^{-1}(\tan\beta/\cos\alpha) \tag{17}$$

or for small sideslip angles,

$$\Delta\theta_{LE} = \beta \sec\alpha \tag{18}$$

[#] For the 6% thick wing $\alpha_{2Ds} = 12°$ gives $\alpha_s = 5.7°$.

In attached flow, the windward side normal force is increasing because of the increased aspect ratio. Eqs. (1) and (2) give

$$
\begin{aligned}
C_N &\sim K_P \\
K_P &= 2\pi \tan\,\theta_{LE} \cos^2\,\theta_{LE}
\end{aligned}
\tag{19}
$$

Thus, the β-derivative for the normal force of the windward half of the delta wing can be determined as follows:

$$
\left.
\begin{aligned}
\frac{1}{2}\,\frac{1}{C_{Na}}\,\frac{dC_{Na}}{d\beta} &= \frac{1}{2}\,\frac{1}{K_P}\,\frac{\partial K_P}{\partial \theta_{LE}}\,\frac{d\theta_{LE}}{d\beta} \\
\frac{1}{K_P}\,\frac{\partial K_P}{\partial \theta_{LE}} &= \cot\,\theta_{LE} - \tan\,\theta_{LE} \\
\frac{d\theta_{LE}}{d\beta} &= \sec\,\alpha
\end{aligned}
\right\}
\tag{20}
$$

The corresponding rolling moment derivative for the wing half is

$$
\left.
\begin{aligned}
-\frac{1}{2}\,\frac{dC_{\ell a}}{d\beta} &= \frac{1}{2}\,\frac{dC_{Na}}{d\beta}\,\frac{\bar{y}_a}{b} \\
\frac{\bar{y}_a}{b} &= \frac{\bar{\xi}_a\,\bar{\eta}_a}{2}
\end{aligned}
\right\}
\tag{21}
$$

and the derivative for the full delta wing becomes

$$
\frac{dC_{\ell a}}{d\beta} = \frac{\bar{\xi}_a\,\bar{\eta}_a}{2}\,\frac{C_{Na}}{\cos\,\alpha}\,(\cot\,\theta_{LE} - \tan\,\theta_{LE})
\tag{22}
$$

For the attached flow loads, the load distribution remains the same for small sideslip angles. This is not true for the vortex-induced loads, which are determined only by the conditions at the leading edge. The loads given by Eq. (6) are the same regardless of whether it is a swept wing or a delta wing. That is, the presence of the center wing area of the delta wing has no effect on the vortex strength and the vortex-induced loads near the leading edge, given by Eq. (6). It is only needed to realize the vortex entrainment effect, Eq. (7). Thus, the windward half of the delta wing has the following increased load due to the sideslip angle (see Fig. 8).

$$\left.\begin{aligned} \frac{1}{2}\ C_{NV}(\alpha, \beta) &= \frac{1}{2}\ C_{NV}(\alpha, 0)\, S(\alpha, \beta)/S(\alpha, 0) \\ S(\alpha, \beta)/S(\alpha, 0) &= 1 + \beta \sec\alpha\, (\cot\ \theta_{LE} - \tan\ \theta_{LE}) \end{aligned}\right\} \tag{23}$$

That is

$$\frac{1}{2}\left(\frac{dC_{NV}}{d\beta}\right)_{\beta=0} = \frac{C_{NV}}{2\cos\alpha}(\cot\ \theta_{LE} - \tan\ \theta_{LE}) \tag{24}$$

For the 70% of the vortex induced load located near the leading edge, Eq. (6), the effective lever arm $\bar{y}_V$ for the rolling moment is (see Fig. 8).

$$\begin{aligned} \bar{y}_V = \bar{\xi}_V\, c_o \Big[\bar{\eta}_V (\tan\ \theta_{LE} + \beta \sec\alpha) \\ - \beta \sec\alpha\Big]\ \cos(\beta \sec\alpha) \end{aligned} \tag{25}$$

For small sideslip angles β the effective dimensionless lever arm for the windward half of the delta wing is

$$\left(\frac{\bar{y}_V}{b}\right)_{.7} = \frac{\bar{\xi}_V\, \bar{\eta}_V}{2}\left[1 - \frac{1 - \bar{\eta}_V}{\bar{\eta}_V}\ \frac{\beta \cot\ \theta_{LE}}{\cos\alpha}\right] \tag{26}$$

For the 30% of the vortex load caused by entrainment effects the dimensionless lever arm is

$$\left(\frac{\bar{y}_V}{b}\right)_{.3} = \frac{\bar{\xi}_a\, \bar{\eta}_a}{2} \tag{27}$$

The β-derivative of the rolling moment for the windward half of the delta wing is

$$-\frac{1}{2}\frac{dC_{\ell V}}{d\beta} = \frac{0.7}{2}\frac{dC_{NV}}{d\beta}\left(\frac{\bar{y}_V}{b}\right)_{.7} + \frac{0.7}{2} C_{NV}\frac{\partial}{\partial\beta}\left(\frac{\bar{y}_V}{b}\right)_{.7} + \frac{0.3}{2}\frac{dC_{NV}}{d\beta}\left(\frac{\bar{y}_V}{b}\right)_{.3} \tag{28}$$

Eqs. (24) – (28) define the following rolling moment derivative for the vortex induced loads on a delta wing

$$-\left(\frac{dC_{\ell V}}{d\beta}\right)_{\beta=0} = \frac{C_{NV}}{2\cos\alpha}\cot\theta_{LE}\left\{0.7\,\bar{\xi}_V\left[(2-\tan^2\theta_{LE})\,\bar{\eta}_V - 1\right] + 0.3\,\bar{\xi}_a\,(1-\tan^2\theta_{LE})\,\bar{\eta}_a\right\} \tag{29}$$

The roll stability derivative given by Eqs. (22) and (29) in combination with Eqs. (5) and (8) is compared with experimental data (Ref. 27) in Fig. 9. The agreement is excellent, substantially better than for Polhamus' theory (Refs. 6 and 27).#

2.4 Mach Number Effects

At sonic speed Jones' slender wing theory (Ref. 8) applies. Thus, the whole wing is effective, i.e., $A_{TE} = 0$ and the "plateauing" does not occur. The attached load distribution along the center chord is as follows for $M_\infty = 1$.

$$\frac{1}{2}\frac{dC_{Na}}{d\xi} = \frac{\pi\sin 2\alpha\tan^2\theta_{LE}}{(b/2c_o)} \qquad \xi : 0 \le \xi \le 1.0 \tag{30}$$

The corresponding vortex induced load distribution is

$$\left.\begin{aligned} \frac{1}{0.7}\frac{1}{2}\frac{dC_{NV}}{d\xi} &= \begin{cases} 1.72\,\pi\,\xi\,\sin^2\alpha & : 0 \le \xi \le 0.4 \\ 0.685\,\pi\,\sin^2\alpha & : 0.4 < \xi \le 1.0 \end{cases} \\ \frac{1}{0.3}\frac{1}{2}\frac{dC_{NV}}{d\xi} &= 1.05\,\pi\,\xi\sin^2\alpha \quad : 0 \le \xi \le 1.0 \end{aligned}\right\} \tag{31}$$

#It should be noted that the present theory is of semi-empirical nature, whereas Polhamus' theory is of the pure variety.

Integration gives the following aerodynamic characteristics of a delta wing at $M_\infty = 1.0$

$$\left.\begin{aligned}
C_{Na} &= \pi (A/2) \sin\alpha \cos\alpha \\
C_{ma} &= -(c_o/\bar{c})\, C_{Na}\, (\bar{\xi}_a - \xi_{CG}) \\
C_{NV} &= \pi \sin^2\alpha \sec^2\theta_{LE} \\
C_{mv} &= -(c_o/\bar{c})\, C_{NV}\, (\bar{\xi}_V - \xi_{CG}) \\
\bar{\xi}_a &= 0.667 \;:\; \bar{\xi}_V = 0.587
\end{aligned}\right\} \qquad (32)$$

An obvious way to make a smooth transition from $M_\infty = 0$ to $M_\infty = 1.0$ in regard to A_{TE} is the following

$$A_{TE} = (A_{TE})_{M_\infty = 0} \sqrt{1 - M_\infty^2} \qquad (33)$$

Applying the same smoothening also to the load distribution gives the following unified representation of the subsonic longitudinal aerodynamic characteristics of a delta wing.

$$\left.\begin{aligned}
C_{Na} &= \pi (A/2) \sin\alpha \cos\alpha \left(1 - 0.09 \sqrt{1 - M_\infty^2}\right) \\
&\quad (1 - \sin^2\theta_{LE} \sqrt{1 - M_\infty^2} \\
C_{ma} &= -(c_o/\bar{c})\, C_{Na}\, (\bar{\xi}_a - \xi_{CG}) \\
C_{NV} &= \pi \sin^2\alpha \sec^2\theta_{LE} \\
&\quad \left(1 - \sin^2\theta_{LE} \sqrt{1 - M_\infty^2}\right) \\
C_{mV} &= -(c_o/\bar{c})\, C_{NV}\, (\bar{\xi}_V - \xi_{CG}) \\
\bar{\xi}_a &= \left(0.667 - 0.027 \sqrt{1 - M_\infty^2}\right) \\
&\quad \left(1 - \bar{\eta}_a \sin^2\theta_{LE} \sqrt{1 - M_\infty^2}\right) \\
\bar{\xi}_V &= \left(0.587 - 0.027 \sqrt{1 - M_\infty^2}\right) \\
&\quad \left(1 - \bar{\eta}_V \sin^2\theta_{LE} \sqrt{1 - M_\infty^2}\right)
\end{aligned}\right\} \qquad (34)$$

The unsteady aerodynamics are given by Eqs. (10) and (13) also at $M_\infty \neq 0$ if Eq. (9) is substituted by

$$\frac{c_{eff.}}{c_o} = \left[(1 - 0.09 \sqrt{1 - M_\infty^2})(1 - \sin^2 \theta_{LE} \sqrt{1 - M_\infty^2})(2 - \cos^{-2} \alpha_o)\right]^{1/2} \tag{35}$$

$C_{N\alpha V}$, $\overline{\xi}_a$ and $\overline{\xi}_V$ are obtained from Eq. (34)

The expressions for the rolling moment derivative remain the same as before, Eqs (22) and (26).

Figure 10 shows that the longitudinal aerodynamic characteristics of a delta wing at subsonic speeds predicted by Eq. (34) are in excellent agreement with experimental data (Ref. 27). Combining Eq. (34) with Eqs. (21) and (28) gives the predicted rolling moment derivatives at $\beta = 0$. Figure 11 shows that these are also in good agreement with the experimental results (Ref. 27).

It is of considerable interest to know how far into the supersonic region this approach based on Jones' slender wing theory (Ref. 8) can be carried. Brown (Ref. 28) has shown that the slender wing theory gives increasing over-prediction of the lift for increasing apex angle and increasing Mach number (Fig. 12). The results in Figure 12 are well approximated by the following expression.

$$K_M = C_{L\alpha}/(C_{L\alpha})_{SL.W.} = 1.00 - \begin{cases} 0 & : 0 \leq \dfrac{\tan \theta_{LE}}{\tan \mu} \leq 0.06 \\ 0.10 \left(\dfrac{\tan \theta_{LE}}{\tan \mu} - 0.06\right) & : \dfrac{\tan \theta_{LE}}{\tan \mu} > 0.06 \end{cases} \tag{36}$$

Polhamus' expression (Ref. 7) for the effect of supersonic Mach numbers on the vortex lift can after some algebra be written as follows

$$\frac{K_V (M_\infty > 1)}{K_V (M_\infty = 1)} = K_M^{\,2} \sqrt{1 - \left(\frac{\tan \theta_{LE}}{\tan \mu}\right)^2} \tag{37}$$

When the leading edge goes supersonic, $\tan \theta_{LE} = \tan \mu$, the vortex lift disappears, as it should.

With these results the longitudinal aerodynamic characteristics of a delta wing can be determined as follows for supersonic speeds, $M_\infty > 1$.

$$\left.\begin{aligned} C_{Na} &= \pi K_M (A/2) \sin \alpha \cos \alpha \\ C_{ma} &= -(c_o/\bar{c})(0.667 - \xi_{CG}) C_{NA} \\ C_{NV} &= \pi K_M^{\,2} \sin^2 \alpha \sec^2 \theta_{LE} \sqrt{1 - \left(\frac{\tan \theta_{LE}}{\tan \mu}\right)^2} \\ C_{mV} &= -(c_o/\bar{c})(0.587 - \xi_{CG}) C_{NV} \end{aligned}\right\} \tag{38}$$

The unsteady aerodynamics are given by Eqs. (10) and (13) provided that Eq. (9) is substituted by

$$\frac{c_{eff.}}{c_o} = \left[K_M (2 - \cos^{-2} \alpha_o)\right]^{1/2} \tag{39}$$

Combining Eqs. (37) and (39) with Eqs. (22) and (29) gives the rolling moment derivative $C_{\ell\beta}$ for supersonic speeds.

At high supersonic speeds, where the leading edge flow is supersonic, another analytic approach is needed. The unsteady embedded Newtonian flow theory (Refs. 29 and 30) can provide the basis for prediction of the attached flow loads, on top of which separated flow effects can be superimposed (Ref. 24).

2.5 Effect of Trailing Edge Sweep

The delta wing analysis can be extended to apply to slender wings with swept leading and trailing edges. Two equivalent delta wings are defined, one for the attached flow loads and another for the vortex induced loading (see Fig. 13). The equivalent delta wing characteristics are referenced to the slender wing geometry using the following ratios[#]

$$\left.\begin{aligned} S^*/S &= (1 - \tan\,\theta_{LE} \tan\,\theta_{TE})/(1 - \bar{\eta}\,\tan\,\theta_{LE} \tan\,\theta_{TE})^2 \\ c^*_o/c_o &= 1/(1 - \bar{\eta}\,\tan\,\theta_{LE} \tan\,\theta_{TE}) \\ b^*/b &= (1 - \tan\,\theta_{LE} \tan\,\theta_{TE})/(1 - \bar{\eta}\,\tan\,\theta_{LE} \tan\,\theta_{TE}) \end{aligned}\right\} \qquad (40)$$

Figures 14 and 15 show that the low speed longitudinal and lateral stability characteristics predicted by use of Eq. (40) in combination with the delta wing expressions, Eqs. (4), (7), (22), and (29), agree well with experimental results (Ref. 27). It is apparent that the present method offers a definite improvement over the Polhamus theory, especially in regard to the arrow wing characteristics. This is true also at high speed, $M_\infty = 0.8$ (Figs. 16 and 17).

[#]The star indicates parameter values for the equivalent delta wing.

Section 3
ORBITER UNSTEADY AERODYNAMICS

The space shuttle orbiter has a wing of double-delta planform (Fig. 18). An 80° swept inner delta wing, a strake, is preceding the 45° swept main delta wing. It is well known that the strake vortex induces a load on the main wing (See Fig. 19 and Refs. 31-33). At high angles of attack the strake and main wing vortices may combine to form one (large-core) vortex (Ref. 32). In absence of a fuselage the downstream strength of the strake vortex, determining the magnitude of the vortex induced loads, would be the integrated result of the angle of attack distribution along the strake leading edge. However, in the presence of the orbiter fuselage (Fig. 18) the flow situation changes dramatically. At low angles of attack a corner separation occurs at the wing-fuselage juncture which reaches all the way to the strake apex already at moderate angles of attack. The corner separation is vented via a vortex which affects the lift over the aft wing. When the separation occurs at the strake apex, the situation is similar to that for free-body vortices on slender bodies of revolution (Refs. 34, 35, 38 and 39). For the shuttle this means that crossflow at the strake apex determines the proximity of the vortex core to the aft wing, thereby determining the aft wing lift. Thus the situation is very much different from the one dealt with earlier in the pure delta wing analysis.

3.1 Rigid Body Dynamics

The rigid body dynamics of the orbiter (Fig. 18) are computed in the following manner. An equivalent slender wing is defined for computation of the attached flow unsteady aerodynamics, similarly to what was done in the delta wing analysis earlier. The trailing edge of the equivalent wing is located such that the computed slender wing force derivative $C_{N\alpha}$ at $\alpha = 0$ agrees with the measured $C_{N\alpha}$. The vortex induced loads are defined as the difference at angle of attack between actually measured static characteristics (Refs. 36 and 37) and the computed attached flow characteristics. In this manner the flow complications caused by the fuselage are accounted for in regard to the magnitude of the vortex induced loads. In order to obtain the unsteady aerodynamics one has to determine the phasing of these loads.

From the earlier discussion it appears reasonable to lump the crossflow effects on the strake-fuselage vortex to the strake apex. That is, the strake-fuselage vortex is like a free body vortex (Refs. 34, 35, 38 and 39), or a partial span vortex (Refs. 4 and 40), and one can assume that $\overline{U} = U_\infty$. Thus, the lift generated by the strake-fuselage vortex at a station $x-x_A$ downstream of strake apex is determined by the cross flow at the strake apex a time instant Δt earlier, where $\Delta t = (x-x_A)/U_\infty$. This analysis is carried out in detail in Part II of the present report (Ref. 21). The dynamic characteristics computed in this manner are shown in Figures 20 and 21. The agreement with experimental results (Ref. 41) is good, not only at subsonic speeds (Fig. 20) but also in the transonic speed region (Fig. 21). Note the opposite effects on dynamic and static stability of the separation induced loads. In the transonic speed region (Fig. 21) shock-boundary layer interactions complicate the picture. However, also the shock-induced flow separation is to a large extent controlled by the strake-fuselage vortex (Ref. 21). Thus, the cross flow at the strake apex determines also the shock-induced separated flow effects on the vehicle dynamics.

3.2 Aeroelastic Characteristics

The rigid body dynamic data for the orbiter shown in Figure 22 for $M_\infty = 1.2$ reveal that a dramatic change of flow pattern occurs at $\alpha \approx 8°$. The measured large increase of dynamic stability and corresponding moderate decrease of static stability are typical for nonlinear, possibly discontinuous, aerodynamic characteristics which are associated with suddenly increased flow separation, such as has been observed on slender cone-cylinder bodies (Ref. 42). This accounted for the 1% (of critical) loss of damping measured on the Saturn-Jupiter nose shroud (See Fig. 23 and Refs. 42 and 43). Whether this sudden increase of the flow separation will increase or decrease elastic vehicle damping depends entirely on the mode shape. Figure 24a shows how one of the candidate straight wings for the early space shuttle configuration experienced undamping (negative damping) at $M_\infty = 0.85$ (Ref. 44). Figure 24b shows the measured vibration response for a slightly different wing.* However, on the swept wing of a high performance aircraft a sudden change of the shock-induced separation pattern causes increased damping (Fig. 25 and Ref. 46). That the wing bending response still increases in this case is the result of the increased forcing function, the buffet input. It is the combined effect of the forcing function and the change of aerodynamic damping that determines the buffet response (Ref. 47)

Figure 26 shows the similar effects of sudden separation on cone-cylinder bodies (Ref. 48) and two-dimensional airfoils (Ref. 19). A force couple is generated together with a net negative normal force, which may be more pronounced in the two-dimensional flow case. Figure 27 illustrates how this net negative force would produce a statically destabilizing and hence damping effect on the rigid body orbiter, oscillating in pitch, all in agreement with the results shown in Figure 23. The effect for the elastic mode sketched in Figure 27 will be the opposite with the force couple providing a statically restoring and hence undamping moment. It should be noted that it is the force couple that does the damage to the aeroelastic damping. Thus, if the resultant net force had been of negligible magnitude the rigid body dynamic data would not have given any warning about this possibility of aeroelastic instability. The question is then, whether or not the actual orbiter can experience such large adverse aeroelastic effects. Flow visualization photographs (Ref. 49) indicate that this can indeed be the case. The nodal line for the first torsional mode, as obtained from Reference 50#, is delineated

*Actually the fin for the same straight wing space shuttle configuration, (Ref. 45). The peak response is, therefore, at $M_\infty = 0.90$ and not at $M_\infty = 0.85$.

#Note that the flutter investigation in Reference 50 was performed at $\alpha = 0$ and $\alpha = 3°$, i.e., far from the critical α-range for sudden separation changes.

in Figure 28. One notices that the separation line moves from a position aft of the nodal line to a position far forward of the nodal line when the angle of attack is increased from $\alpha = 5°$ to $\alpha = 10°$.

When combining the information presented in Figures 22 through 28 one becomes convinced that large adverse aeroelastic effects will be experienced by the orbiter wing at certain critical combinations of angle of attack and Mach number. Figure 29 shows how this critical angle of attack varies with Mach number and cone angle for cone-cylinder bodies (Refs. 47 and 48). Within the α_{crit}-range shown the flow alternated between the two separated flow patterns. This would indicate that the adverse aeroelastic effect can be realized for a range of angles of attack $\alpha = \alpha_{crit} \pm \Delta\alpha_{crit}$, as is also verified by the results obtained with the Jupiter nose shroud (Fig. 23). α_{crit} and, in particular, $\Delta\alpha_{crit}$ are very sensitive to Reynolds number. One can, of course, expect the critical angle of attack region for the orbiter wing to be equally sensitive to Reynolds number. In addition, elevon deflection will strongly influence α_{crit} for the orbiter.

The orbiter wing with its highly swept leading edges is subject to strong three-dimensional flow effects. How the wing sweep affects the shock-boundary layer interaction has been studied thoroughly (See Ref. 51). The similarity with the flow pattern on the orbiter wing (Ref. 49) is apparent in Figure 30. In addition to this triple-shock complication, the wing sweep also introduces a unique boundary layer transition behavior with associated decisive effects on the flow separation patterns. The spanwise flow, with its propensity for the development of an inflexion point in its boundary layer profile (Ref. 52), causes the flow to become turbulent on the outer wing panel while it is still laminar inboard. For some ranges of Mach number and angle of attack this causes the outboard wing to have a region of attached leading edge flow with retarded shock-induced separation (see Fig. 31 and Ref. 53). At a certain angle of attack the separation jumps to the leading edge causing a dramatic change of the flow field over the complete wing. How this critical angle of attack varies with leading edge sweep for TACT-F111 (Refs. 54 and 55) is shown in Figure 32. The F111 wing with its supercritical airfoil and built-in 4 degrees "wash-out" at the wing tips does experience the flow pattern shown in Figure 31, whereas the orbiter with its more conventional airfoil shape does not. (Fig. 28). That is, on the orbiter the separation does not jump all the way to the leading edge when α exceeds α_{crit}. Otherwise, α_{crit} for the orbiter fits into the general trend shown by the TACT-F111 (see Fig. 32).

Unfortunately there are no flow pictures available for the orbiter without OMS-pods. Without the restraining action from the pod shock the separation probably moves farther aft before it jumps forward. Whether or not it jumps all the way to the leading edge is a moot question. In any case, the discontinuous force change will be larger than in the presence of the OMS-pods. This explains the much larger damping measured on the "clean" orbiter (see Fig. 22). It is also in agreement with the observed large effect of pod geometry on the complete wing flow field (see Fig. 33 and Ref. 49). It is obvious that at a sideslip angle α_{crit} will be different for the up-wind and down-wind wing halves. That is, the snap roll problem encountered on the straight-winged early orbiter configuration (Refs. 56-58) could be of concern also for the present orbiter. The wing tip loads dominate the rolling moment and have an even larger effect on the wing root bending moment (Ref. 59). In addition to sideslip, control deflections can have very large effects on elastic and rigid body dynamics (Refs. 27, 35 and 56). During launch the interference flow effects from HO-tank and SRM-rockets are large even when not considering the effects of rocket plumes (see Ref. 60 and Vol. II of the present report). Adding to all this complexity is the fact that it is very difficult to simulate shock boundary layer interaction even in the simple case of a straight wing (see Fig. 34 and Refs. 61-63). When considering the three-dimensional aspects (Figs. 31-34) the problem becomes even more formidable.

Section 4
CONCLUSIONS

A study of the steady and unsteady aerodynamics of the space shuttle orbiter has given the following results.

- The effect of Mach number for a subsonic leading edge is accounted for by a simple modification of Jones' slender wing theory for the attached flow loads and by a reformulation of Polhamus' theory for the vortex induced loads.
- The effect of leading edge roundness is largely accounted for by considering the delay of leading edge separation in the cross flow plane due to leading edge roundness.
- The effect of trailing edge sweep (forward or back) is well predicted by use of two equivalent delta wings, one for the attached flow loads and another for the vortex induced loads.
- Both pitch and roll stability derivatives, determined by the presented closed form solutions, are in excellent agreement with available experimental data.
- The slender wing analysis can be extended to the orbiter wing with its double-delta plan form wing by defining two equivalent wings.

  The attached flow loads are given by an equivalent slender wing that gives the measured $C_{N\alpha}$ at $\alpha = 0$.

  The vortex induced loads are defined as the difference at $\alpha > 0$ between measured total loads and computed attached flow loads. The cross flow at the strake apex is controlling the unsteady effects of the vortex induced loads.
- The unsteady aerodynamics of the orbiter computed in this manner are in good agreement with measured dynamic characteristics in the whole Mach number range investigated, $0.3 \leq M_\infty \leq 1.2$.

- In the transonic speed region, $0.9 \leq M_\infty \leq 1.2$, the space shuttle orbiter is subject to vortex-shock-boundary layer interactions which cause highly nonlinear or discontinuous changes of the aerodynamic loads when a critical angle of attack is exceeded. It is found that this could have a strongly adverse effect on the aeroelastic stability of the wing in its lowest torsional mode. This flow phenomenon can also have a dramatic effect on the vehicle dynamics, with the possibility of snap roll being of some concern.
- The vortex-shock-boundary layer interaction is extremely sensitive to model surface roughness and free stream Reynolds number, and it appears impossible to simulate it in a wind tunnel test unless full scale Reynolds number can be reached. This is not possible with present ground test facilities, at least not with the size model needed for the complicated space shuttle. For these reasons the following approach is suggested.

  Obtain consistent static and dynamic data for a "nominal current" configuration including "current" OMS-pods and the operational range of control deflections.

  Conduct parametric tests to determine incremental effects of geometric changes, control deflection, sideslip, etc. as well as of surface roughness and Reynolds number.

  Develop analytic means by which the wind tunnel test results can be predicted thereby ensuring confident analytic extrapolation to full scale conditions.

Obviously the investigation outlined above should be broad enough to enable the analyst to find "fixes" as needed to ensure structural integrity and acceptable vehicle dynamics.

REFERENCES

1. Ericsson, L.E. and Reding, J.P., "Report on Saturn I-Apollo Unsteady Aerodynamics," LMSC A650215, Contract NAS 8-5338, Lockheed Missiles & Space Company, Sunnyvale, Ca., Feb. 1964.

2. Ericsson, L.E. and Reding, J.P., "Analysis of Flow Separation Effects on the Dynamics of a Large Space Booster," J. Spacecraft & Rockets, Vol. 2, No. 4 July-Aug., 1965, pp. 481-490.

3. Rainey, A.G., "Progress on the Launch Vehicle Buffeting Problem," J. Spacecraft & Rockets, Vol. 2, No. 3, May-June, 1965, pp. 289-299.

4. Ericsson, L.E. and Reding, J.P., "Unsteady Aerodynamic Analysis of Space Shuttle Vehicles, Part I: Summary Report," Report LMSC/D352320, Part I, Contract NAS 8-28130, Lockheed Missiles & Space Company, Inc., Sunnyvale, California, Aug. 1973.

5. Ericsson, L.E., and Reding, J.P., "Unsteady Aerodynamic Analysis of Space Shuttle Vehicles, Part II: Steady and Unsteady Aerodynamics of Sharp-Edged Delta Wings," Report LMSC/D352320, Part II, Contract NAS 8-28130, Lockheed Missiles & Space Company, Inc., Sunnyvale, California, Aug. 1973.

6. Ericsson, L.E. and Reding, J.P., "Unsteady Aerodynamics of Slender Delta Wings at Large Angles of Attack," J. Aircraft, Vol. 12, No. 9, Sept. 1975, pp. 721-729.

7. Polhamus, E.C., "Predictions of Vortex-Lift Characteristics by a Leading-Edge Suction Analogy," Journal of Aircraft, Vol. 8, No. 4, Apr. 1971, pp. 193-199.

8. Jones, R.T., "Properties of Low-Aspect-Ratio Pointed Wings at Speeds Below and Above the Speed of Sound," Report No. 835, May 1945, NASA.

9. Elle, B.J., "An Investigation at Lo.v Speed of the Flow Near the Apex of Thin Delta Wings with Sharp Leading Edges, "R&M 3176, Aeronautical Research Council, Great Britain, Jan. 1958.

10. Lambourne, N.C., Bryer, D.W., and Maybrey, J. F. M. "Pressure Measurements on a Model Delta Wing Undergoing Oscillatory Deformation," NPL Aero Report 1314, Aeronautical Research Council, Great Britain, March 1970.

11. Woodgate, L., "Measurements of the Oscillatory Pitching Moment Derivatives on a Delta Wing with Round Leading Edges in Incompressible Flow," R&M No. 3628, Part 1, July 1968, Aeronautical Research Council, Great Britain.

12. Woodgate, L. and Pugh, P.G., "Measurements of the Pitching-Moment Derivatives on a Sharp-Edged Delta Wing in Incompressible Flow," R&M No. 3379, Aeronautical Research Council, Great Britain, 1963.

13. Gersten, K., "Nichtlineare Tragflächen Theorie insbesondere für Tragflügel mit kleinen Sietenverhältnis, "Igenieur-Archiv, Vol. 30, 1961, pp. 431-452.

14. LaMar, J.E., "Prediction of Vortex Flow Characteristics of Arbitrary Wing Planforms at Supersonic Speeds," AIAA Paper No. 75-249, Jan. 1975.

15. Ville, G., "Influence des Decallements au Bord d'Attaque sur les Characteristiques Aerodynamiques des Voilures," Association Francaise de Ingenieurs at Techniciens des l'Aeronautique et de l'Espace, Colloque d'Aerodynamique Appliquée, 4th Lille, France, Nov. 8-10, 1967.

16. Ericsson, L.E. and Reding, J.P. "Unsteady Airfoil Stall and Stall Flutter" LMSC A-6J-71-1, Contract NAS 1-9987, Lockheed Missiles & Space Company, Inc., Sunnyvale, Calif., June 1971.

17. Ericsson, L.E. and Reding, J.P., "Stall Flutter Analysis," J. Aircraft, Vol. 10, No. 1, Jan. 1973, pp. 5-13.

18. Jacobs, E.N. and Sherman, A. "Airfoil Section Characteristics as Affected by Variations in the Reynolds Number," Tech. Report 586 (1937). NACA

19. Lindsey, W.F. and Landrum, E.J. "Compilation of Information on the Transonic Attachment of Flows at the Leading Edges of Airfoils," TN 4204, Feb. 1958. NACA

20. Nichols, M.E., "Results of Investigations on the 0.004 Scale Model 74-0 of the Configuration 4 (Modified) Space Shuttle Orbiter in the NASA/MSFC 14 by 14 inch Trisonic Wind Tunnel (0A131)," NASA CR 141, 521, March 1975.

21. Reding, J.P. and Ericsson, L.E., "Unsteady Aerodynamic Flow Field Analysis of the Space Shuttle Configuration; Part II; Launch Vehicle Aeroelastic Analysis," Report LMSC/D057194, Part II, Contract NAS 8-30652, Lockheed Missiles & Space Company, Inc., Sunnyvale, California, April 1976.

22. Reding, J.P. and Ericsson, L.E., "Unsteady Aerodynamic Analysis of Space Shuttle Vehicles, Part IV: Effect of Control Deflections on Orbiter Unsteady Aerodynamics," Report LMSC/D352320, Part IV, Contract NAS 8-28130, Lockheed Missiles & Space Company, Inc., Sunnyvale, Calif. Aug. 1973.

23. Hummel, D. and Srinivasan, P.S., "Vortex Breakdown Effects on the Low-Speed Aerodynamic Characteristics of Slender Delta Wings in Symmetrical Flow," J. Royal Aer. Soc., Vol. 71, No. 4, Apr. 1967, pp. 319-322.

24. Reding, J.P. and Ericsson, L.E., "Delta Wing Separation Can Dominate Shuttle Dynamics," J. Spacecraft and Rockets, Vol. 10, No. 7, July 1973, pp. 421-428.

25. Reding, J.P. and Ericsson, L.E., "Unsteady Aerodynamics Could Dominate the Space Shuttle Aeroelastic Stability," Paper No. 74-362, AIAA/ASME/SAE 15th Structures, Structural Dynamics and Materials Conference, Las Vegas, Nevada, April 17-19, 1974.

26. Ericsson, L.E. and Reding, J.P., "Dynamic Stall Analysis in Light of Recent Numerical and Experimental Results," Journal of Aircraft, Vol. 12, 1975 (see also AIAA Paper No. 75-26).

27. Davenport, E.E. and Huffman, J.K., "Experimental and Analytical Investigation of Subsonic Longitudinal and Lateral Aerodynamic Characteristics of Slender Sharp-Edge 74° Swept Wings," TN D-6344, July 1971, NASA.

28. Brown, C.E., "Theoretical Lift and Drag of Thin Triangular Wings at Supersonic Speeds," Report No. 839, Nov. 1946, NACA

29. Ericsson, L.E., "Generalized Unsteady Embedded Newtonian Flow," Journal of Spacecraft and Rockets, Vol. 12, 1972 (See also AIAA Paper No. 75-210).

30. Ericsson, L.E. "Unsteady Embedded Newtonian Flow," Astronautica Acta, Vol. 18, 1973, pp. 309-330.

31. Wendtz, W.H., and Kohleman, D.L., "Vortex Breakdown on Slender Sharp-Edged Wings," AIAA Paper No. 69-778, July 1969.

32. Wendtz, W.H., Jr. and McMahon, M.C., "An Experimental Investigation of the Flow Fields About Delta and Double-Delta Wings at Low Speeds," NASA CR-521 August 1966.

33. Wendtz, W.H., Jr. and McMahon, M.C., "Further Experimental Investigations of Delta and Double-Delta Wing Flow Fields at Low Speeds," NASA CR 714, February 1967.

34. Reding, J.P. and Ericsson, L.E., "Review of Delta Wing Space Shuttle Vehicle Dynamics," Report LMSC-D243938, Contract NAS 9-11495, Lockheed Missiles & Space Company, Inc., Sunnyvale, California, Oct. 1971.

35. Reding, J.P. and Ericsson, L.E., "Review of Delta Wing Space Shuttle Vehicle Dynamics," Vol. III, Proceedings Space Shuttle Aerothermodynamics Conference, NASA Ames RC, Moffett Field, Calif. Dec. 15-16, 1971 (NASA TM X-2508), pp. 861-931

36. Lindsey, A.I. and Milam, M.D., "Results of Differential Elevon/Aileron Deflection for Lateral Control Optimization and Elevon Hinge Moment Investigations on an 0.015-scale Model (74-0) of the Space Shuttle Orbiter in the NASA/Langley Research Center 8' TPT (0A116), NASA CR 134, 428, Dec. 1974.

37. Allen, E.C., "An Investigation to Verify the Static Stability and Control Effectiveness of the 0.004 Scale Model (74-0) of the Shuttle 5 Orbiter (0A108)," NASA CR 141,537, June 1975.

38. Tobak, M. Schiff, L.B., and Peterson, V.L., "Aerodynamics of Bodies of Revolution in Coning Motion," AIAA Journal, Vol. 7, No. 1, Jan. 1969, pp. 95-99.

39. Pick, G.S., "Side Forces on Ogive-Cylinder Bodies at High Angles of Attack in Transonic Flow," J. Spacecraft and Rockets, Vol. 9, No. 6, June 1972, pp. 389-390. See also AIAA Paper No. 71-570, June 1971.

40. Garner, H.C. and Bryer, D.W., "Experimental Study of Surface Flow and Part-Span Vortex Layers on a Cropped Arrowhead Wing, "R&M No. 3107, Aeronautical Research Council, Great Britain, April 1957.

41. Boyden, R.P. and Freeman, D.C., "Subsonic and Transonic Dynamic Stability Derivatives of a Modified 089B Shuttle Orbiter, "NASA TM X-72631, DMS-DR-2107, Dec. 1974.

42. Ericsson, L.E., "Aeroelastic Instability Caused by Slender Payloads," J. Spacecraft and Rockets, Vol. 4, No. 1, Jan. 1967, pp. 65-73.

43. Hanson, P.W. and Logget, R.V., Jr., "Aerodynamic Damping and Buffet Response of an Aeroelastic Model of the Saturn I Block II Launch Vehicle," TN D-2713 (March 1965). NASA

44. Erickson, L.L., Gambucci, B.J., and Wilcox, P.R., "Initial Transition Flutter Results for a Straight Wing Version of the Space Shuttle Vehicle," NASA SSPD-17, December 15, 1970.

45. Muhlstein, L.J., "Assessment of Potential Buffet Problems on the Space Shuttle Vehicle," Proceedings of NASA Space Shuttle Technology Conference, San Antonio, April 12-14, 1972, TMX-2570, pp. 25-43, NASA

46. Jones, J.G., "The Dynamic Analysis of Buffeting and Related Phenomena," AGARD-CP-102, Paper 23, AGARD Specialists Meeting on Fluid Dynamics of Aircraft Stalling, Lisbon, Portugal, April 25-28, 1972.

47. Ericsson, L.E., "Dynamic Effects of Shock-Induced Flow Separation," J. Aircraft, Vol. 12, No. 2, Feb. 1975, pp. 86-92.

48. Chevalier, H.L. and Robertson, J.E., "Pressure Fluctuations Resulting from Alternating Flow Separation and Attachment at Transonic Speeds," AEDC TDR 63-204 (November 1963).

49. Nichols, M.E., Results of Investigations on the 0.004-Scale Model 74-0 of the Configuration 4 (Modified) Space Shuttle Orbiter in the NASA/MSFC 14- by -14 Inch Trisonic Wind Tunnel (0A131)," NASA-CR-141,521, March 1975.

50. Chipman, R.R. and Rauch, F.J., "Analytical and Experimental Study of the Effects of Wing-Body Aerodynamic Interference on Space Shuttle Subsonic Flutter," NASA CR-2488, Jan. 1975.

51. Lock, R.C. and Rodgers, E. W. E., "Aerodynamic Design of Swept Wings and Bodies for Transonic Speeds," Proceedings of the 2nd International Congress of Aeronautical Sciences, 1960.

52. Owen, P.R., and Randall, D.G., "Boundary Layer Transition on a Swept-Back Wing," Memo No. Aero 277, Royal Aircraft Establishment, Great Britain, June 1952

53. Rogers, E. W. E., Berry, C.J., and Townsend, J. E. C., "A Study of the Effect of Leading Edge Modifications on the Flow Over a 50-Deg Sweptback Wing at Transonic Speeds," Great Brit. R&M No. 3270 (1962).

54. Riddle, D. "TACT Unsteady Aerodynamics," Transonic Aircraft Technology Briefing to Industry and Government, Santa Monica, Calif. Nov. 10, 1975.

55. Riddle, D., "Private Communication of Unpublished Data," NASA Ames Research Center, Moffett Field, Calif. Dec. 12, 1975.

56. Reding, J.P. and Ericsson, L.E. "Review of Delta Wing Space Shuttle Vehicle Dynamics," Report LMSC/D243938, Contract NAS 9-11495, Lockheed Missiles & Space Company, Inc., Sunnyvale, Calif. Oct. 1971.

57. Brownson, J.C., "Static Stability Characteristics of MSC Orbiter Preliminary Tests at Mach No. 0.25-2.0, "NASA SSPD-1, December 22, 1968.

58. Hamilton, E.J. and Ryals, W.G., "Review of 1/10 Scale Space Shuttle Air Drop Test Results," NASA MSC Internal Document 5-2950-1-NOV-126, June 24, 1970.

59. Lambourne, N.C., "Some Remarks on the Aerodynamic Damping Appropriate to Wing Buffeting," Tech. Memo Structures 871, Royal Aircraft Establishment, Great Britain, Aug. 1975.

60. Freeman, D.C., Jr. and Boyden, R.P., "Subsonic and Transonic Dynamic Stability Test Results (R1 Space Shuttle Launch Vehicle)," NASA LA 44.

61. Stanewsky, E. and Hicks, G., "Scaling Effects on Shock-Boundary Layer Interaction in Transonic Flow," AFFDL-TR-68-11, March 1968.

62. Zonars, D. Lowndes, H.B., and Kolb, A.W., "Ground Testing," AIAA Paper No. 68-1084, Oct. 1968.

63. Loving, D.L., "Wind-Tunnel-Flight Correlation of Shock-Induced Separation Flow," TND 3580, 1966. NASA

Appendix A
NOMENCLATURE

A	aspect ratio, $A = b^2/S$
a	speed of sound
A_{TE}	inefficient wing area at $M = 0$ (Fig. 1)
b	wing span
$\bar{c}$	reference length
c_o	slender wing root chord
K_M	Mach number parameter, Eq. (36)
K_P, K_V	potential flow and vortex lift factors, Eq. (1)
K_{P1}	first approximation of K_P
L	lift: coefficient $C_L = L/(\rho_\infty U_\infty^2/2)S$
ℓ	rolling moment: coefficient $C_\ell = \ell/(\rho_\infty U_\infty^2/2)Sb$
M	Mach number: $M = U/a$
M_p	pitching moment: coefficient $C_m = M_p/(\rho_\infty U_\infty^2/2)S\bar{c}$
N	normal force: coefficient $C_N = N/(\rho_\infty U_\infty^2/2)S$ (Fig. 6)
p	static pressure: coefficient $C_p = (p - p_\infty)/(\rho_\infty U_\infty^2/2)$
q	pitch rate
r_N	airfoil nose radius
Re	Reynolds number
S	reference area (= projected wing area)
s	local semi-span

t	time
U	horizontal velocity
$\overline{U}$	convection velocity
x	axial body-fixed coordinate (see inset in Fig. 1)
y	spanwise body-fixed coordinate (see inset in Fig. 1)
α	angle of attack (Fig. 6)
α_o	trim angle of attack
β	sideslip angle (Fig. 6)
$\delta(x, t)$	elastic vehicle deflection, $\delta(x, t) = \phi(x)\, q(t)$
ζ	damping, fraction of critical damping
η	dimensionless y-coordinate, $\eta = y/s$
θ	angular perturbation in pitch
θ_c	cone half angle
θ_{LE}	apex half angle (see inset in Fig. 1)
θ_{TE}	trailing edge sweep angle (Fig. 12)
Λ	leading edge sweep angle, $\Lambda = \pi/2 - \theta_{LE}$
μ	Mach angle, $\mu = \text{cosec}^{-1}(M_\infty)$
ξ	dimensionless x-coordinate, $\xi = (x_A - x)/c_o$
ρ	air density
σ	wing tip acceleration
$\phi(x)$	x-distribution of normalized bending deflection, $\delta(x, t) = \phi(x)\, q(t)$
ω	free-free bending frequency and rigid body pitching frequency
$\overline{\omega}$	reduced frequency, $\overline{\omega} = \omega\, c_o/U_\infty$

Subscripts

A	apex
a	attached flow
CG	center of gravity
crit	critical
d	downstream
eff.	effective
LE	leading edge
max	maximum
N or ⊥	normal to leading edge
s	separated flow
TE	trailing edge
V	vortex
2D	two-dimensional flow
∞	freestream conditions

Superscripts

(*)	trailing edge coordinate, Eq. (39).
(–)	barred quantities denote integrated mean values, e.g., centroid of aerodynamic loads

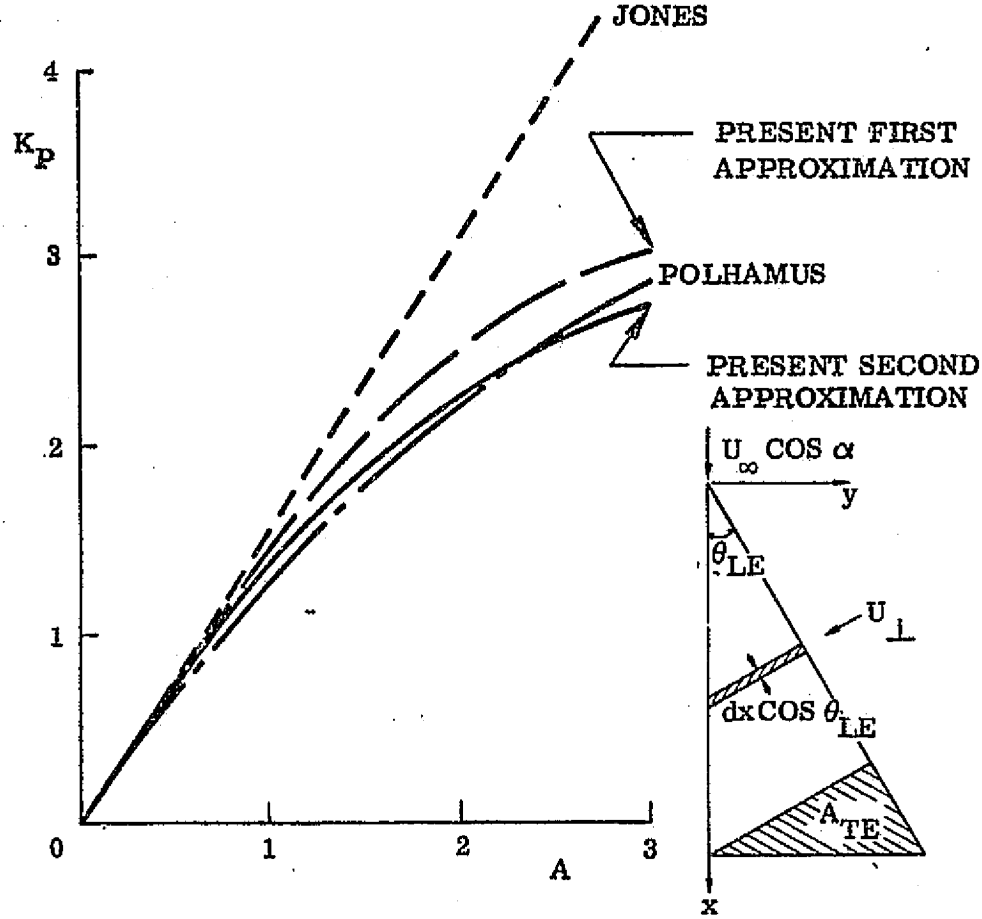

Figure 1 Attached Flow Lift Factor K_p of Delta Wings at $M_\infty = 0$

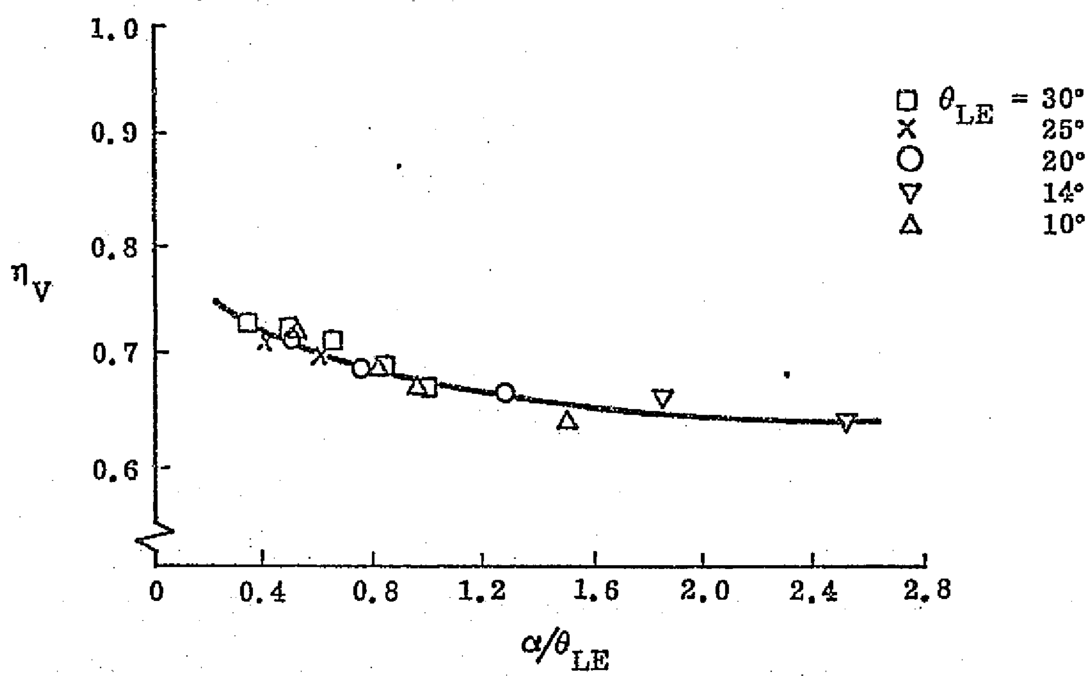

Figure 2 Effect of Leading Edge Sweep on Spanwise Location of Leading Edge Vortex

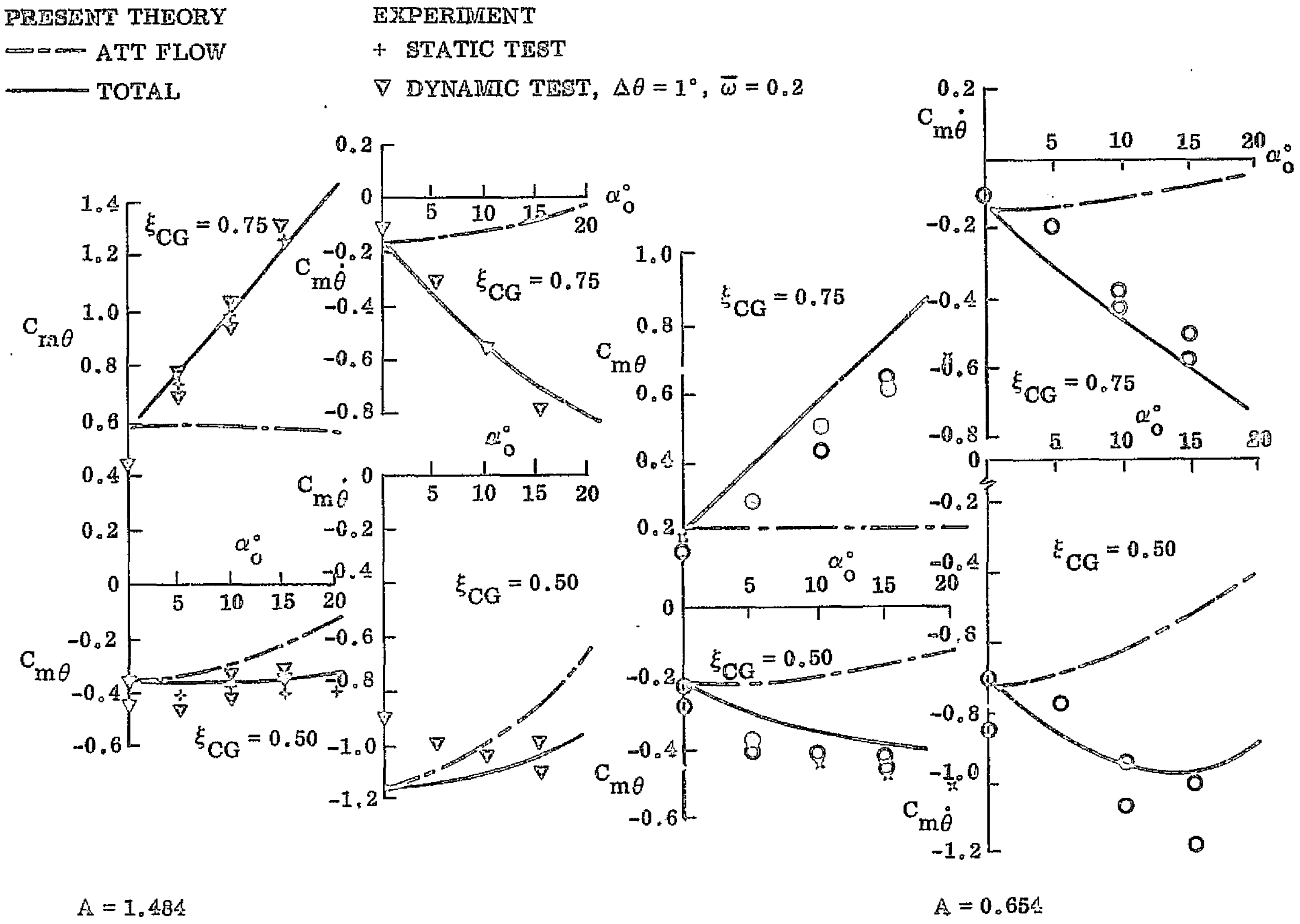

Figure 3 Dynamic Stability Derivatives for Sharp-Edged Delta Wings at $M_\infty = 0$

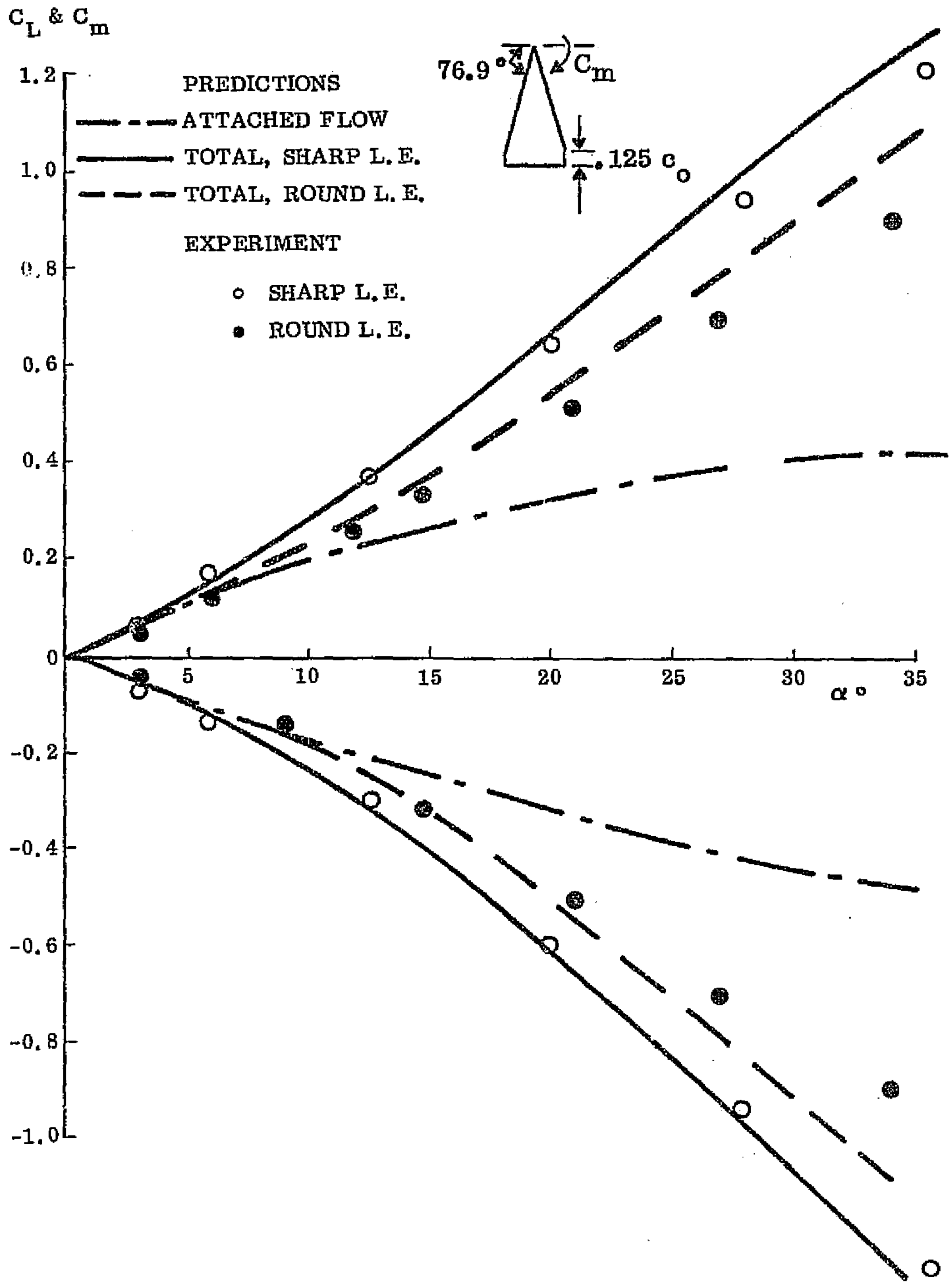

Figure 4 Comparison of Predicted and Measured Effects of Leading Edge Roundness on Static Characteristics of a Slender Wing of Aspect Ratio A = 0.78

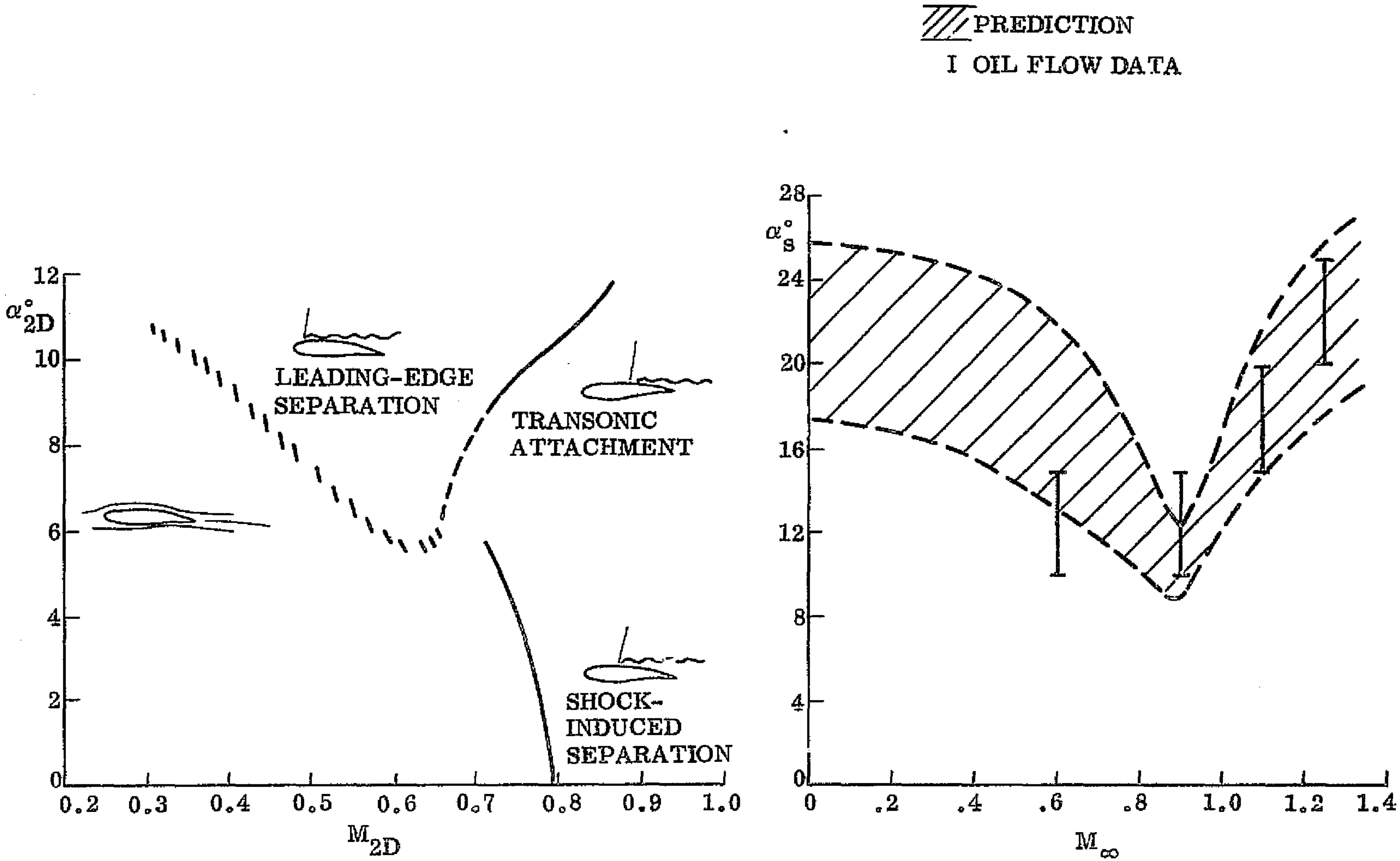

a. Flow Separation Boundary of NACA 64A012 Airfoil

b. Flow Separation Boundary of the Space Shuttle Orbiter

Figure 5 Flow Separation Boundaries

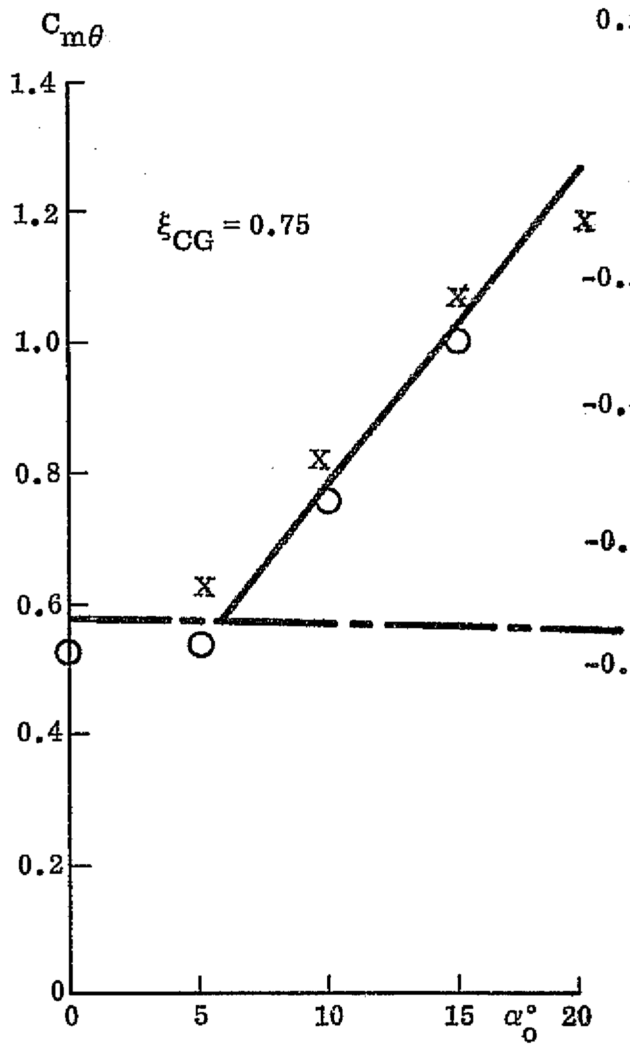

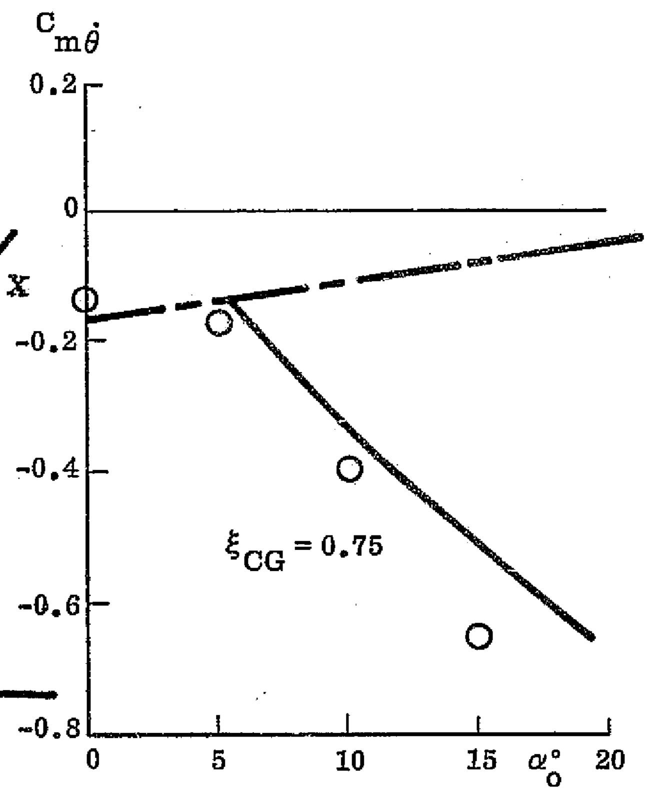

PRESENT THEORY

ATTACHED FLOW

TOTAL

EXPERIMENT

O DYNAMIC TEST, $\Delta\theta$ - 1°, $\bar{\omega} \to 0$

X STATIC TEST

Figure 6 Comparison Between Predicted and Measured Dynamic Stability Characteristics of a Delta Wing With Rounded Leading Edge

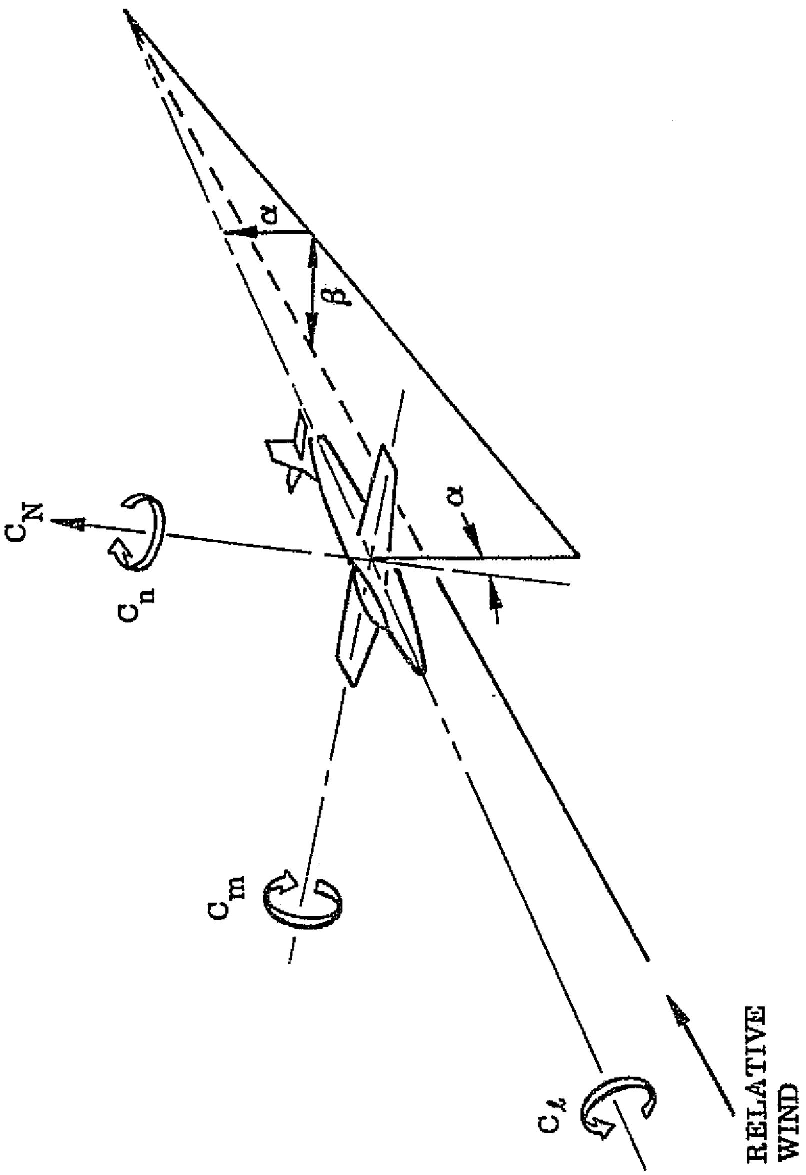

Figure 7 Definition of 6-D Parameters

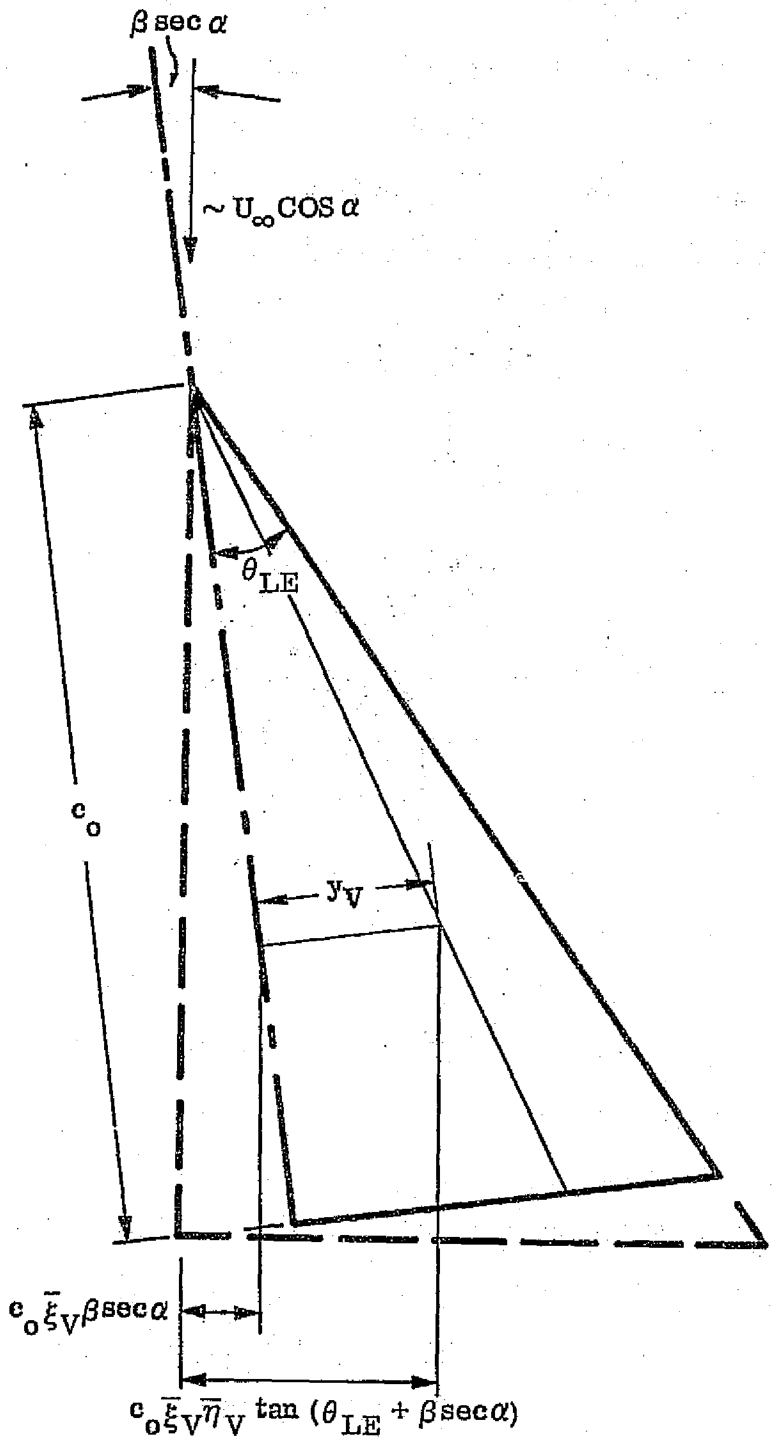

Figure 8 Definition of Yawed Wing Equivalent Geometry

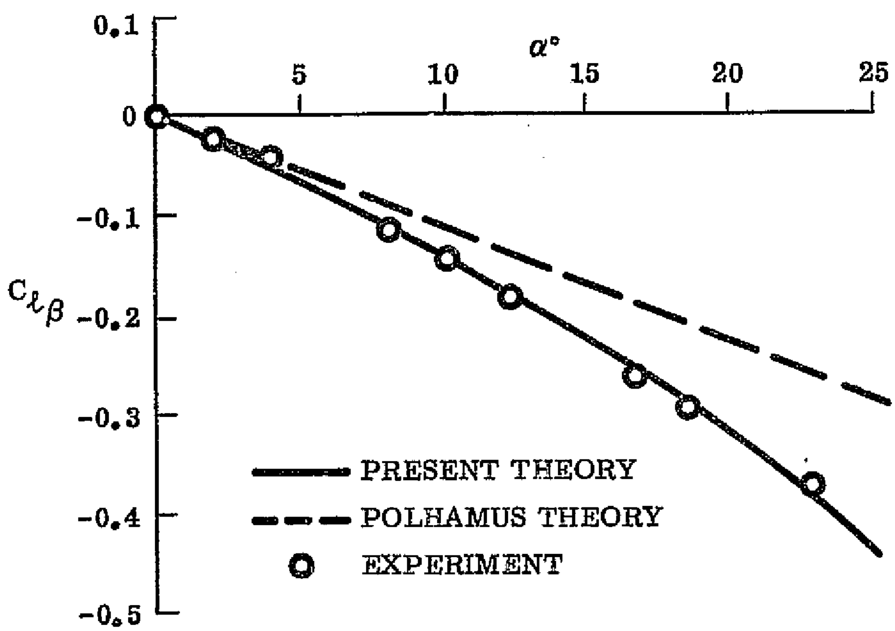

Figure 9 Comparison Between Predicted and Measured Yaw Stability Derivative

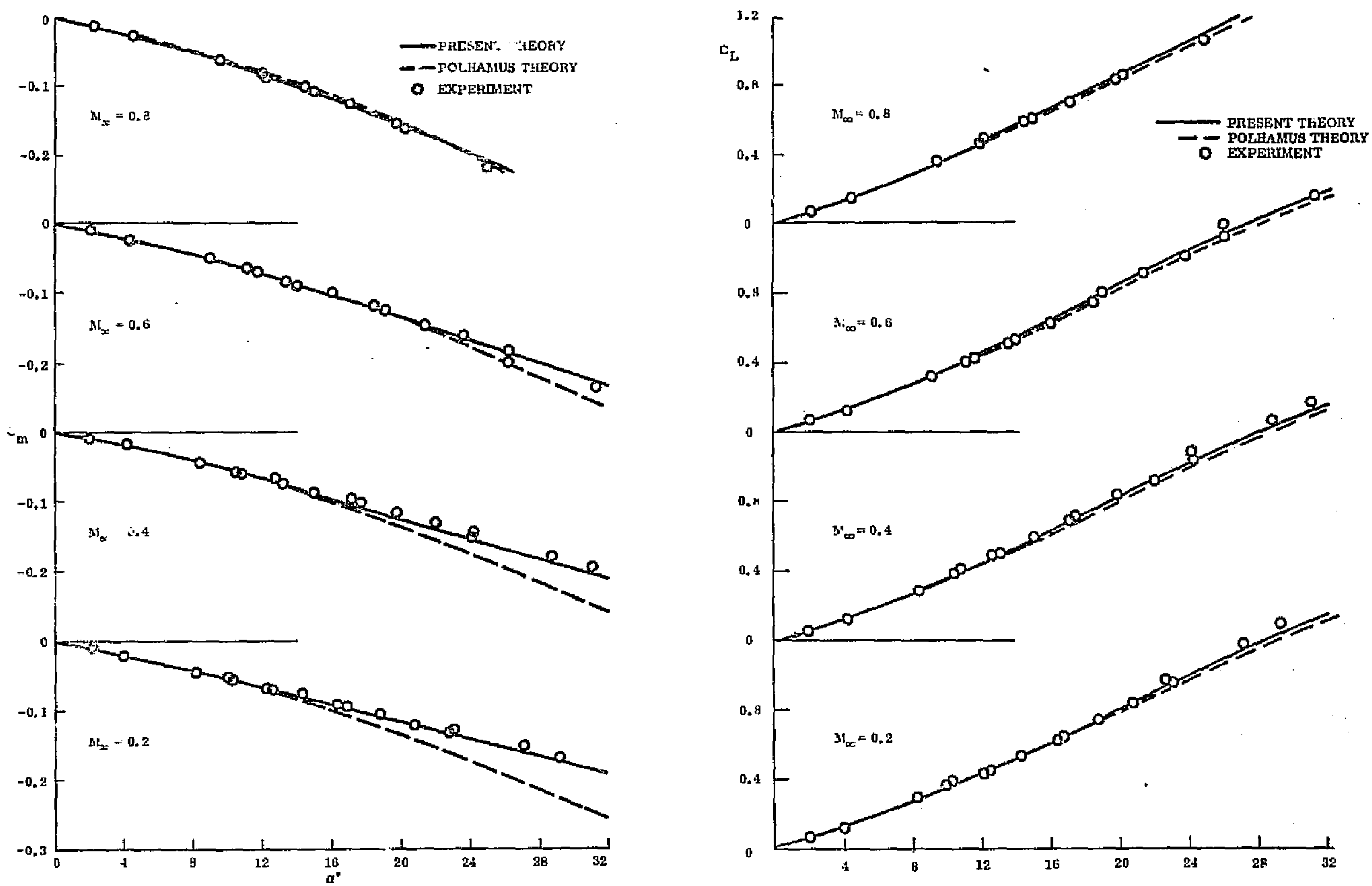

Figure 10 Effect of Mach Number on Longitudinal Delta Wing Aerodynamics

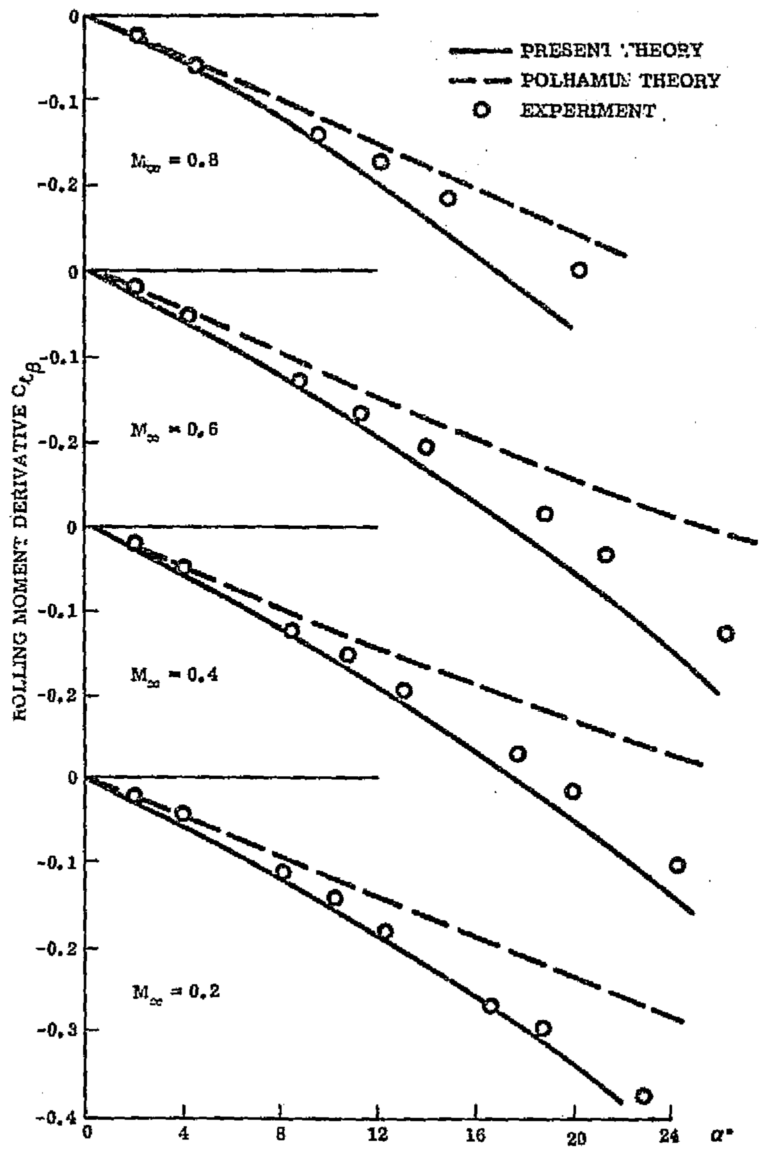

Figure 11 Effect of Mach Number on Lateral Delta Wing Characteristics

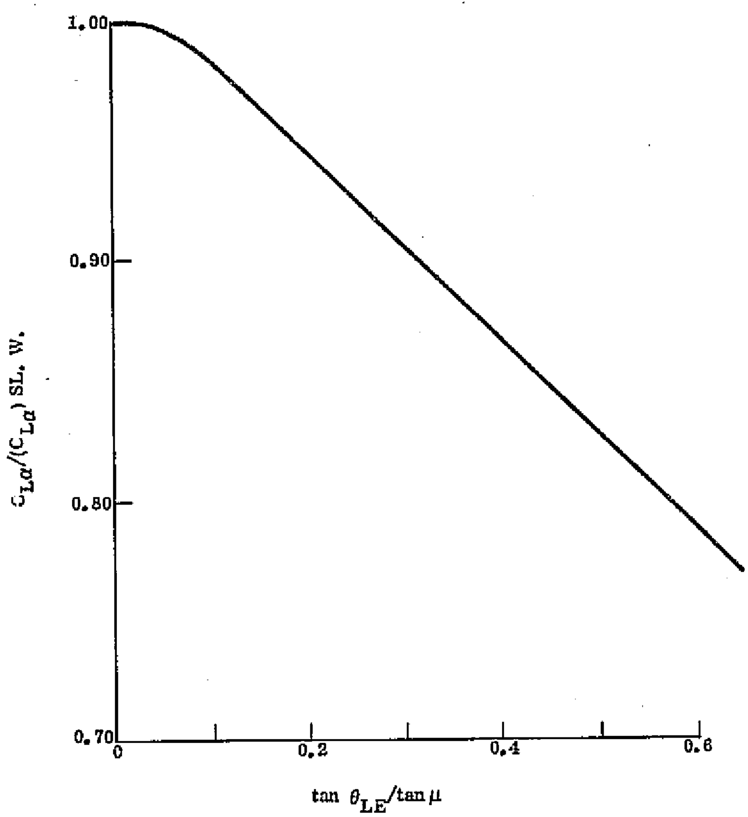

Figure 12 Slender Wing Parameter at Supersonic Speeds

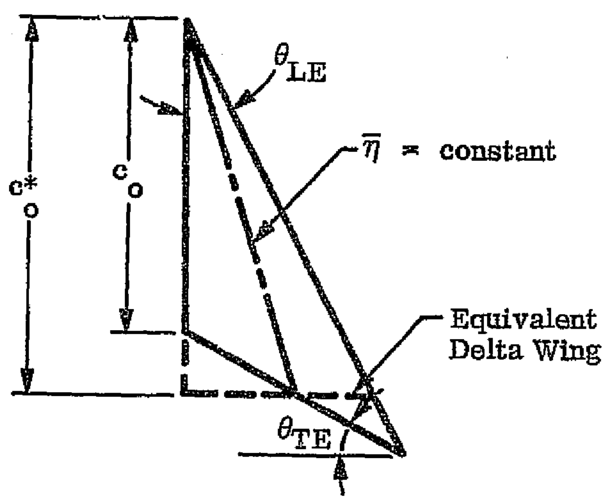

Figure 13 Definition of Trailing Edge Parameters

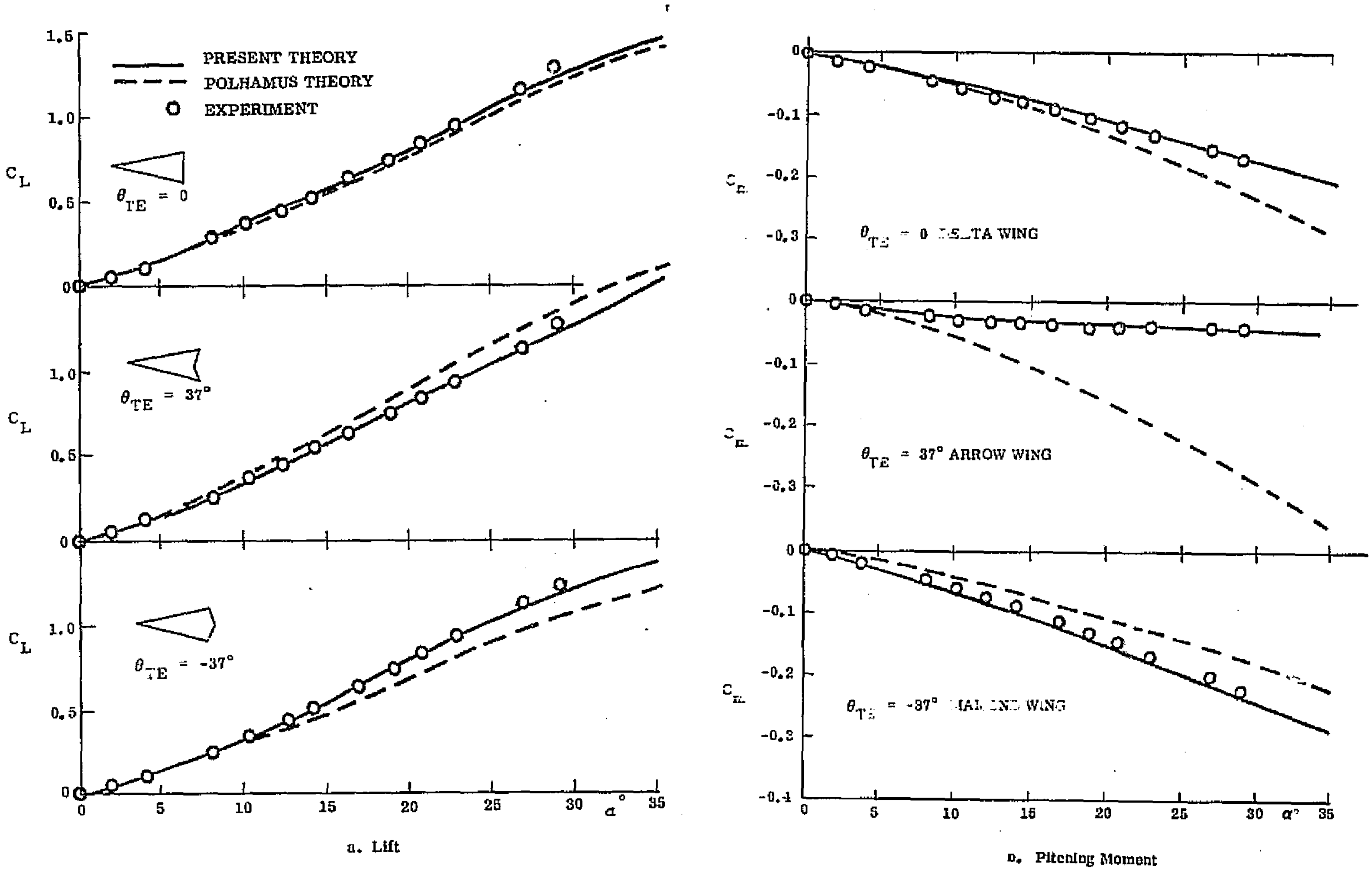

Figure 14 Effect of Trailing Edge Sweep on Longitudinal Aerodynamics at $M_\infty = 0.2$

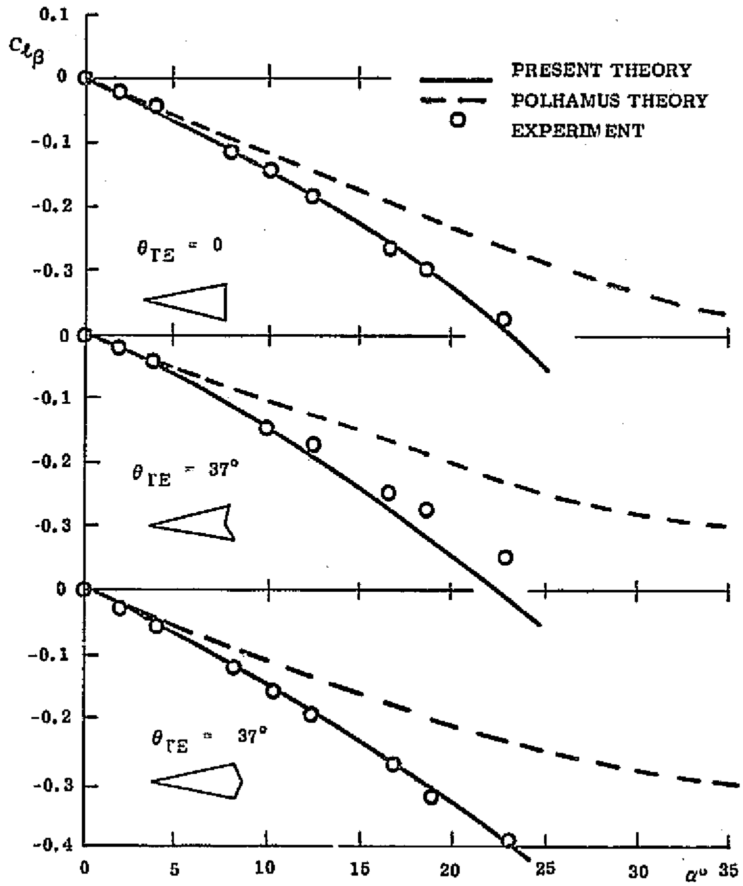

Figure 15 Effect of Trailing Edge Sweep on Lateral Stability at $M_\infty = 0.2$

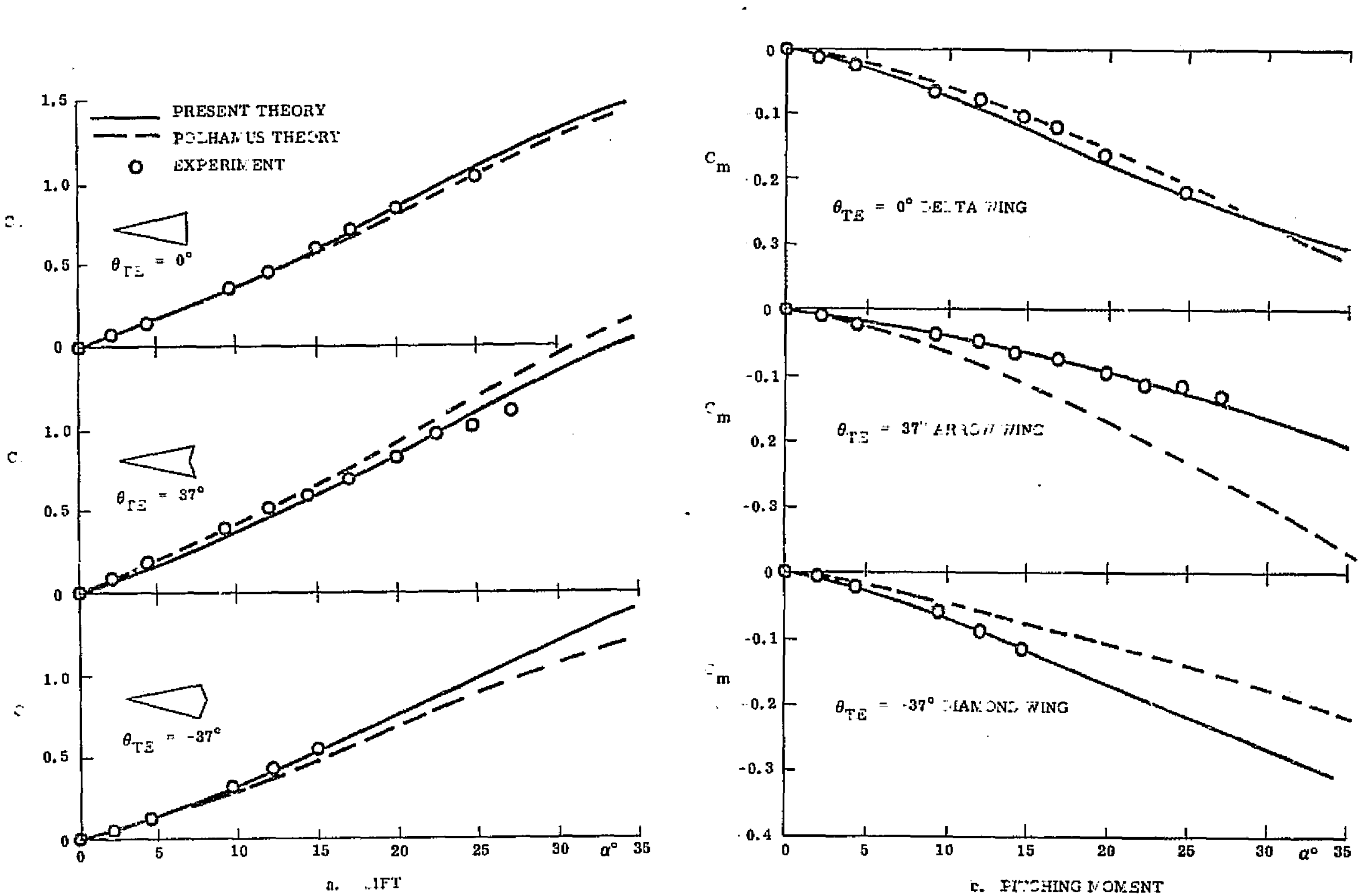

Figure 16 Effect of Trailing Edge Sweep on Longitudinal Aerodynamics at $M_\infty = 0.8$

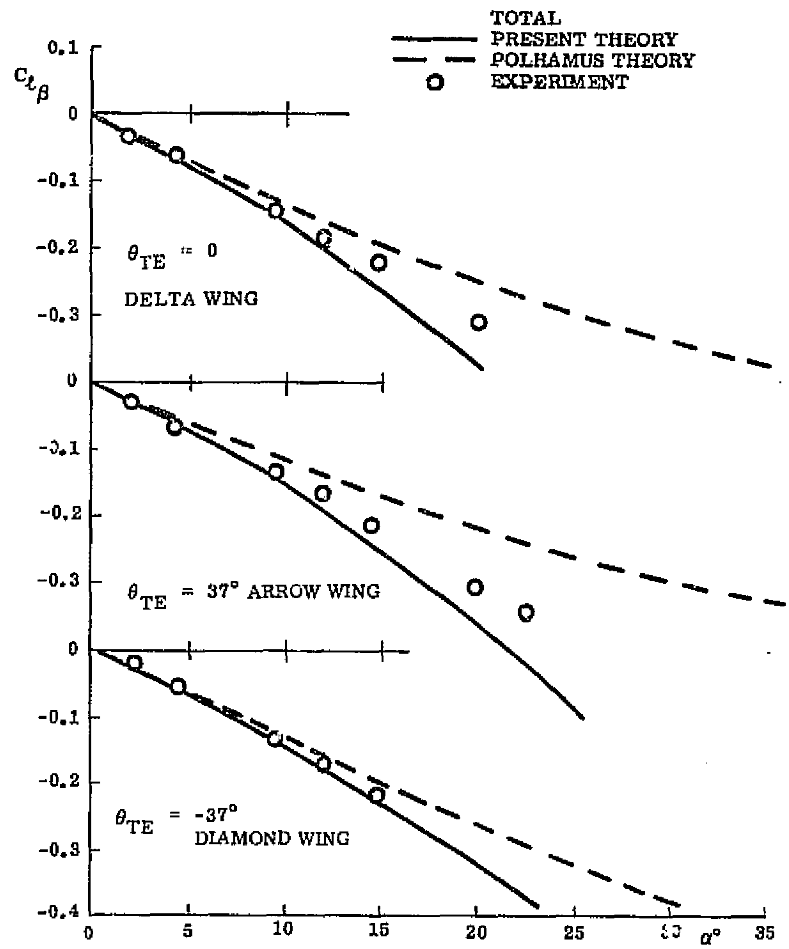

Figure 17 Effect of Trailing Edge Sweep on Lateral Stability at $M_\infty = 0.8$

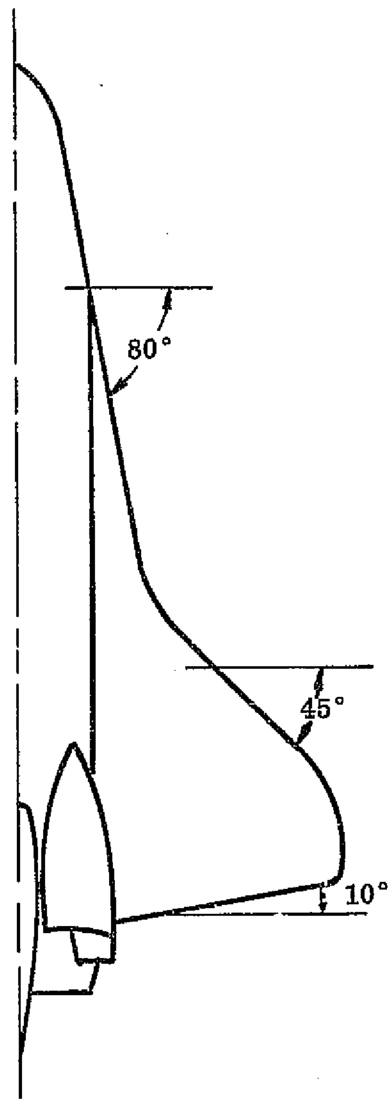

Figure 18 Orbiter Planform

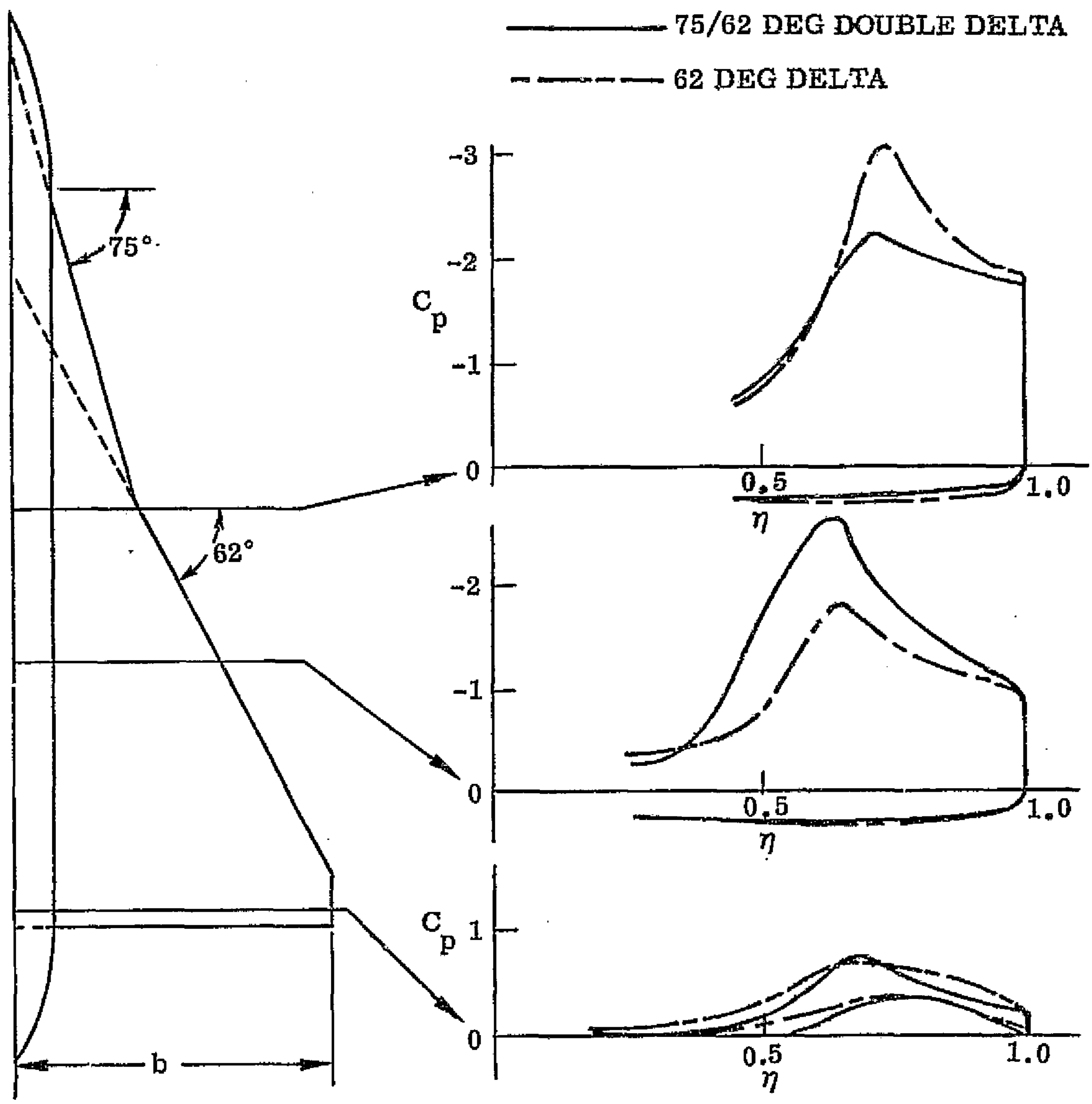

Figure 19 Strake-Induced Loads

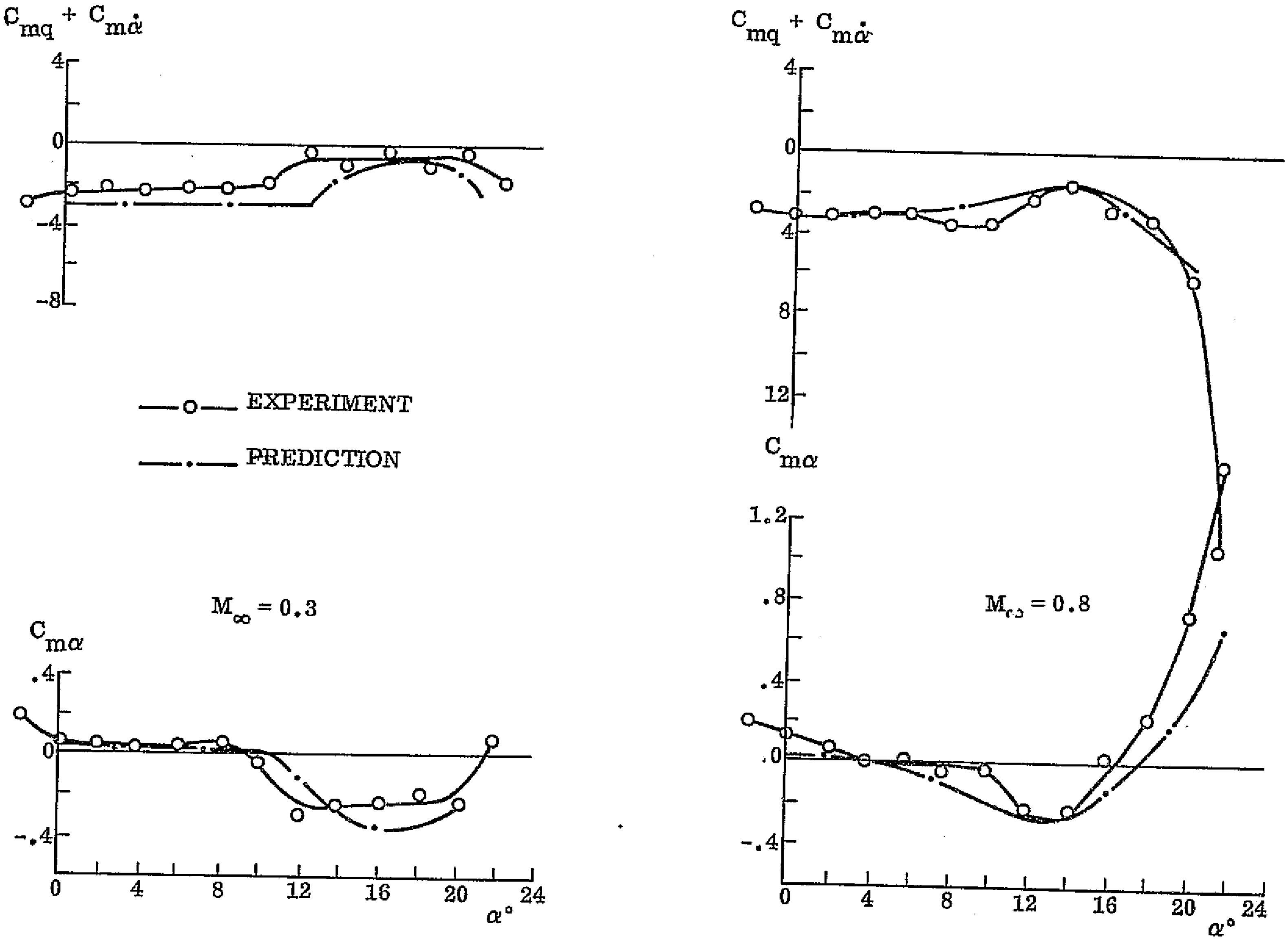

Figure 20 Orbiter Dynamics at Subsonic Speeds

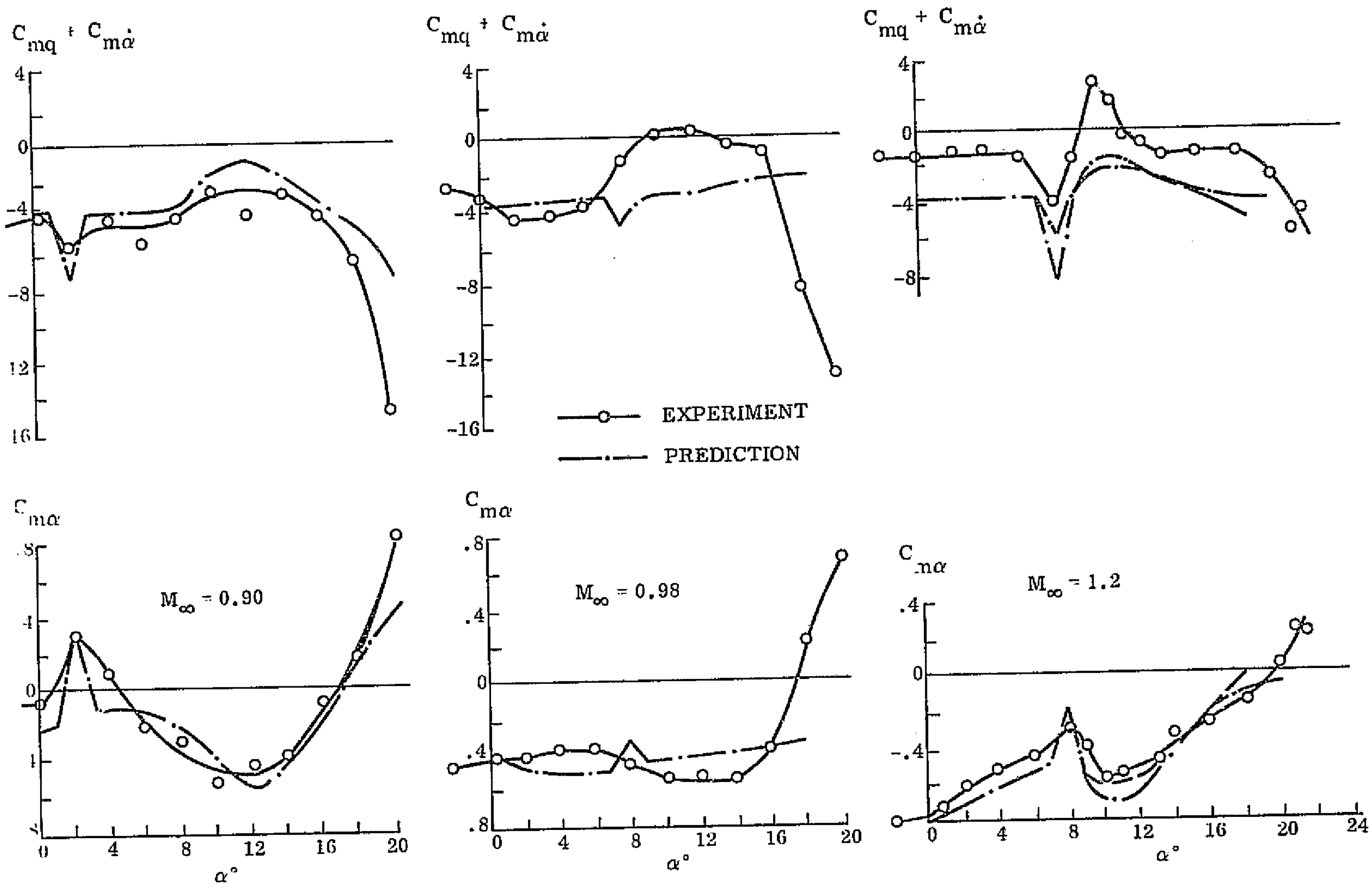

Figure 21 Orbiter Dynamics at Transonic Speeds

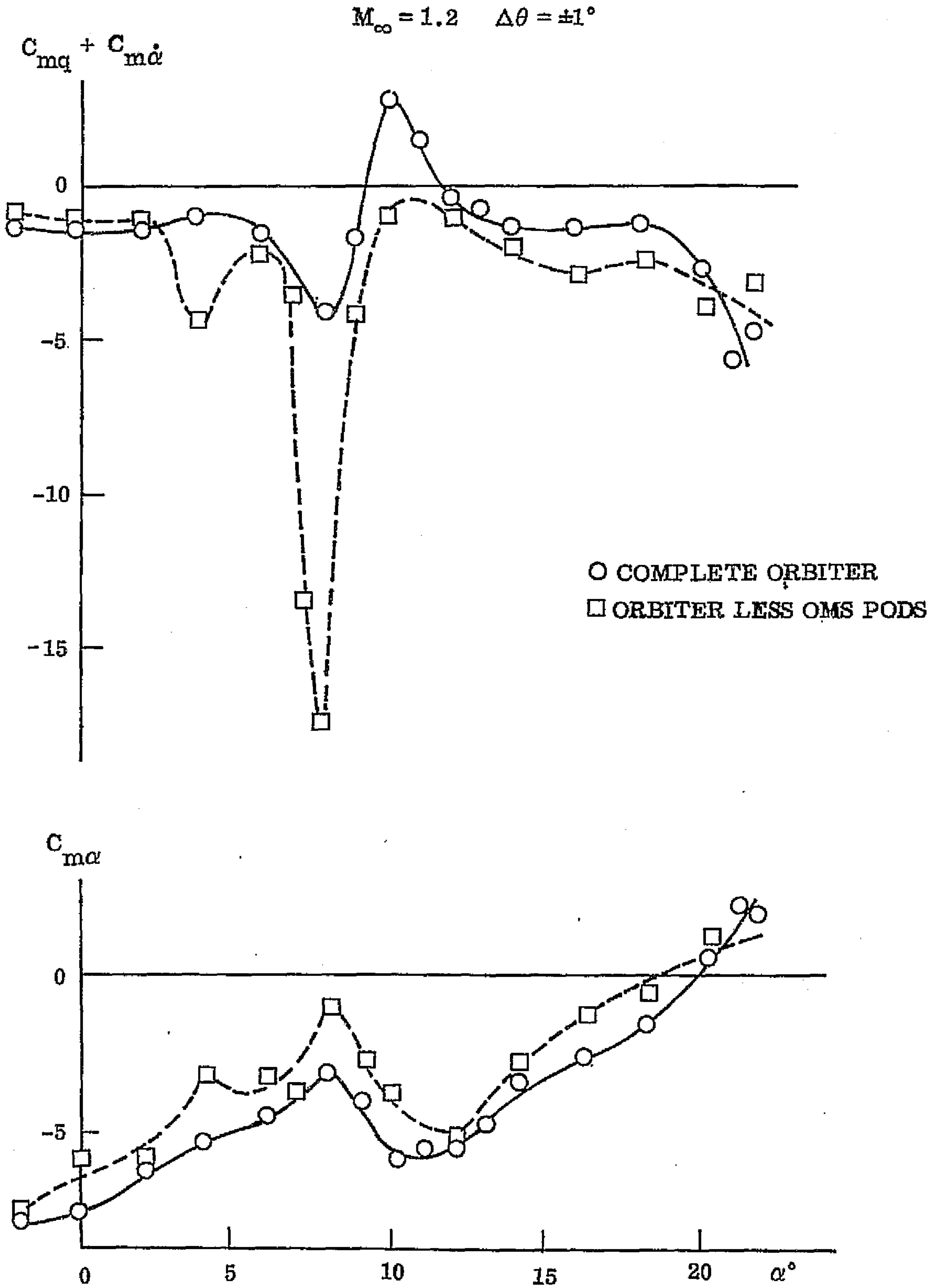

Figure 22 Orbiter Dynamics With and Without OMS-Pods at $M_\infty = 1.2$

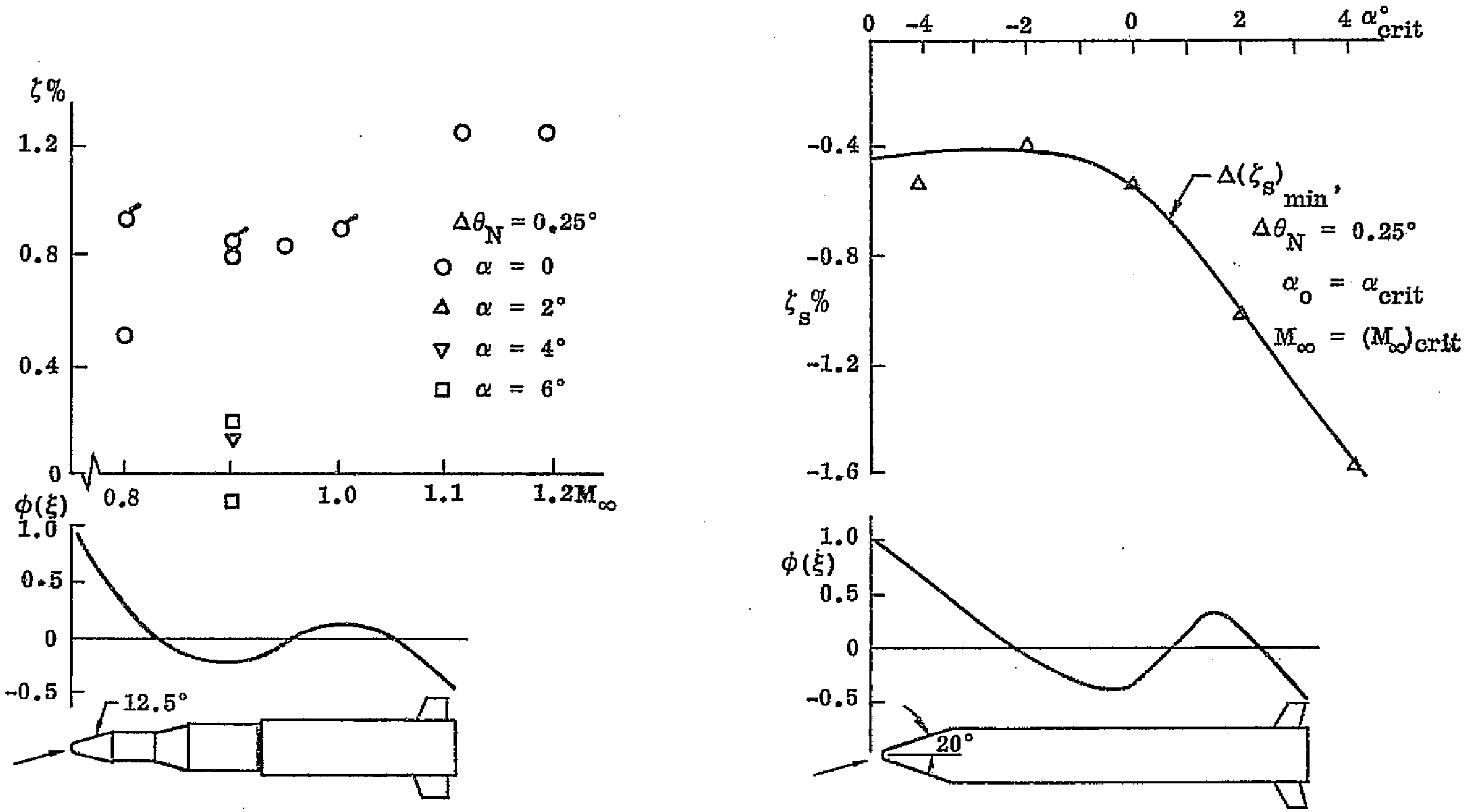

a. Saturn I with a Jupiter Nose Shroud

b. Undamping Induced by Complete Flow Separation

Figure 23 Elastic Vehicle Damping of Slender Cone-Cylinders at High Subsonic Mach Numbers

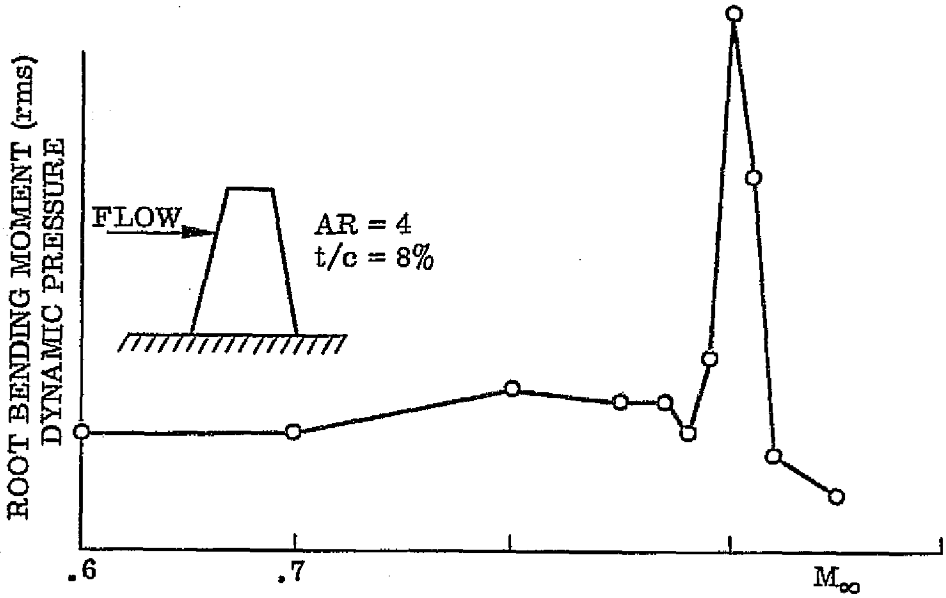

b. Measured Bending Response

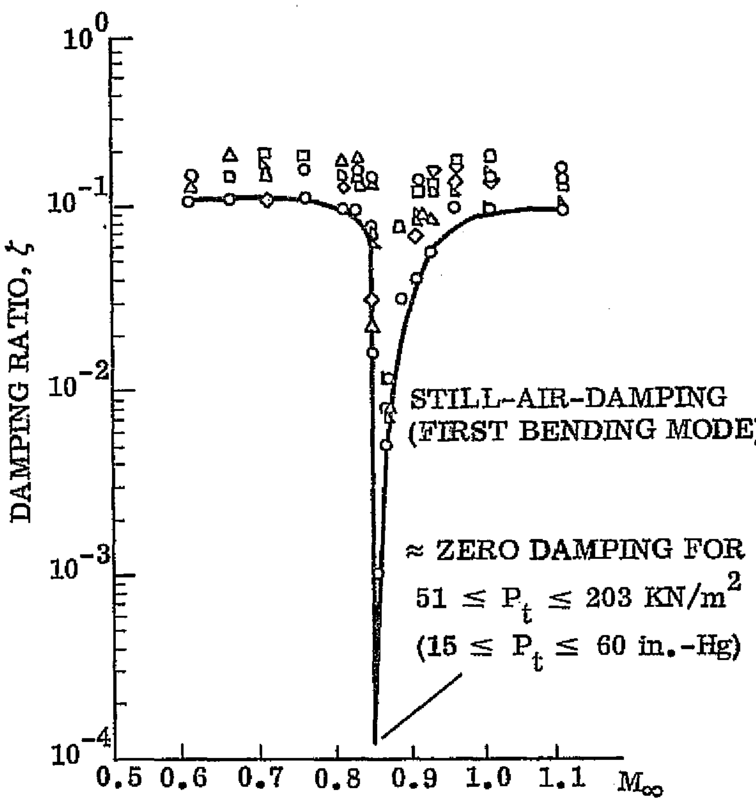

a. Measured Damping

Figure 24 Bending Response and Damping Characteristics of Straight Wings at High Subsonic Mach Numbers

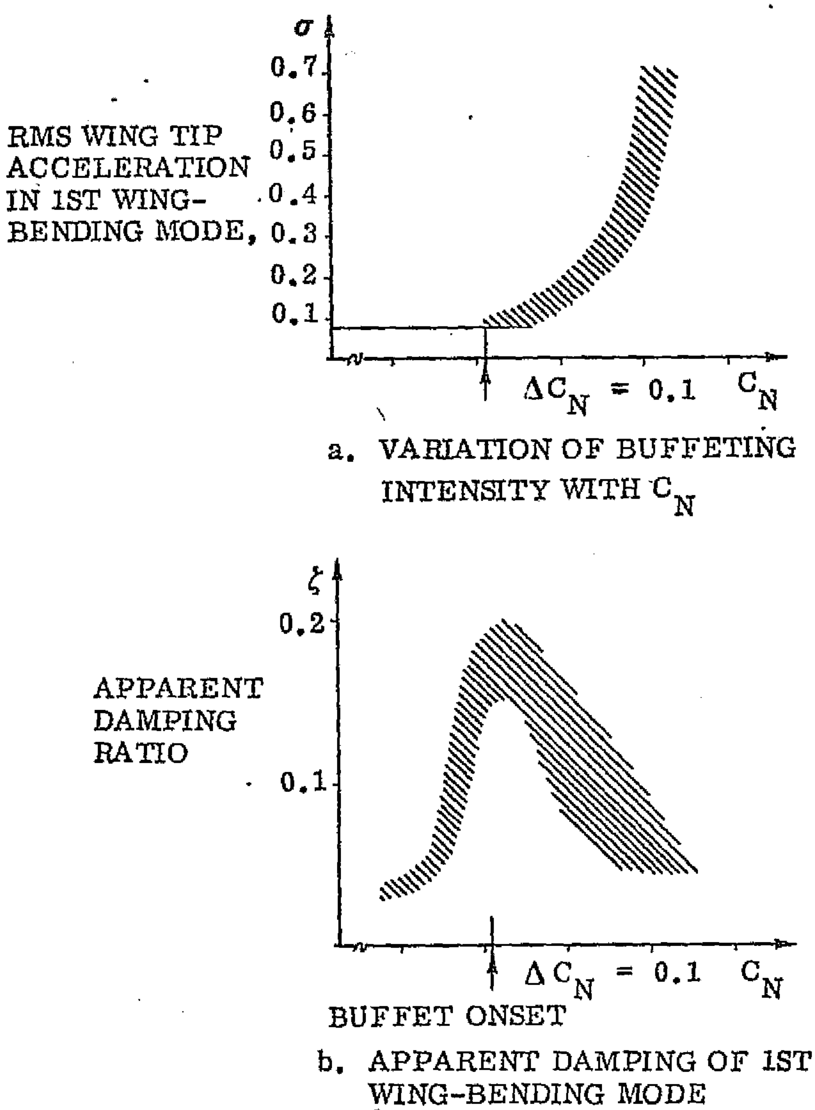

Figure 25 Bending Response and Apparent Aerodynamic Damping of the Swept Wing of a High Performance Aircraft at $M_{\infty} = 0.7$

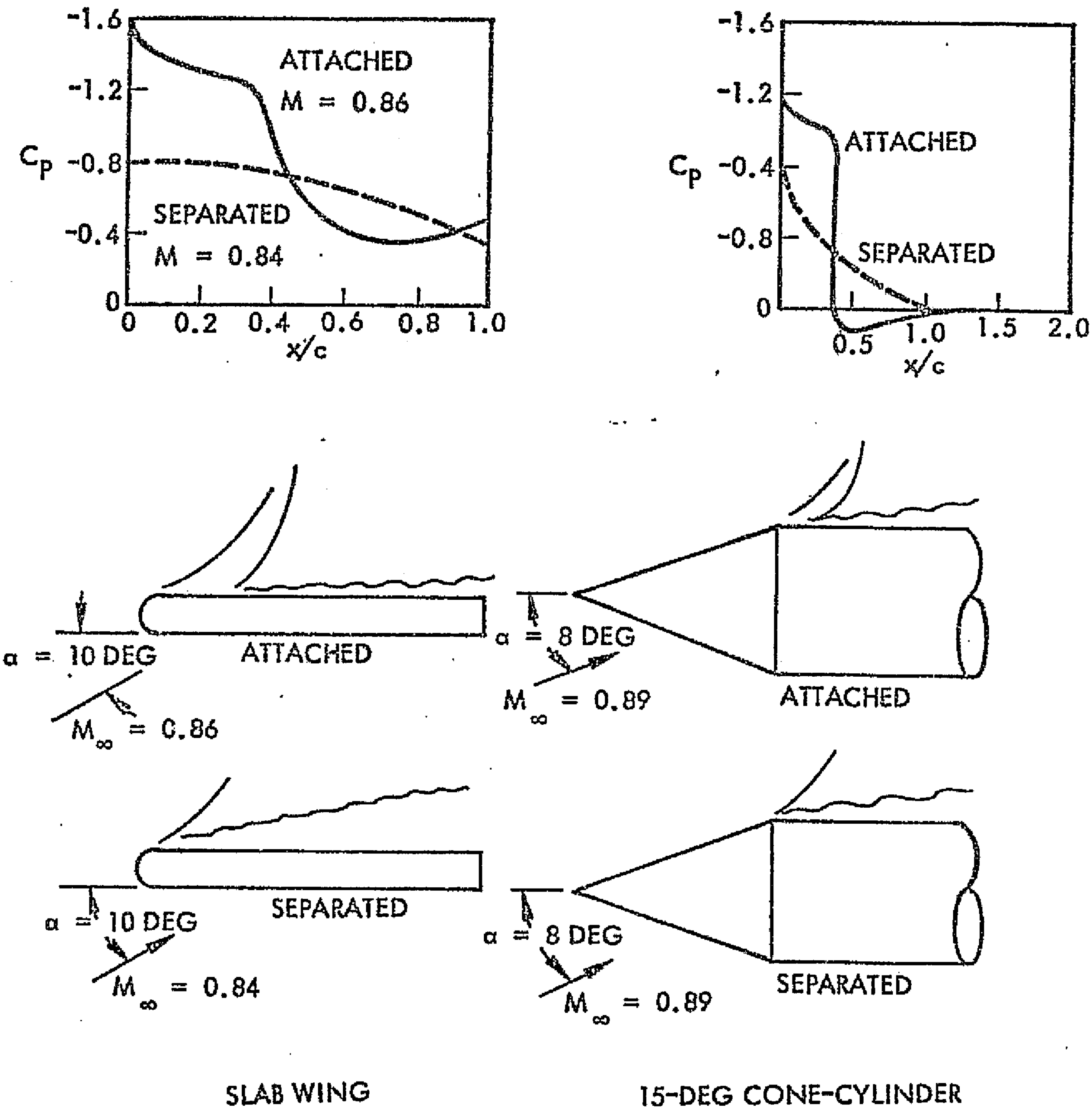

Figure 26 Shock-Induced Separated Flow Loads on a Cone-Cylinder Compared to those on a Slab Wing

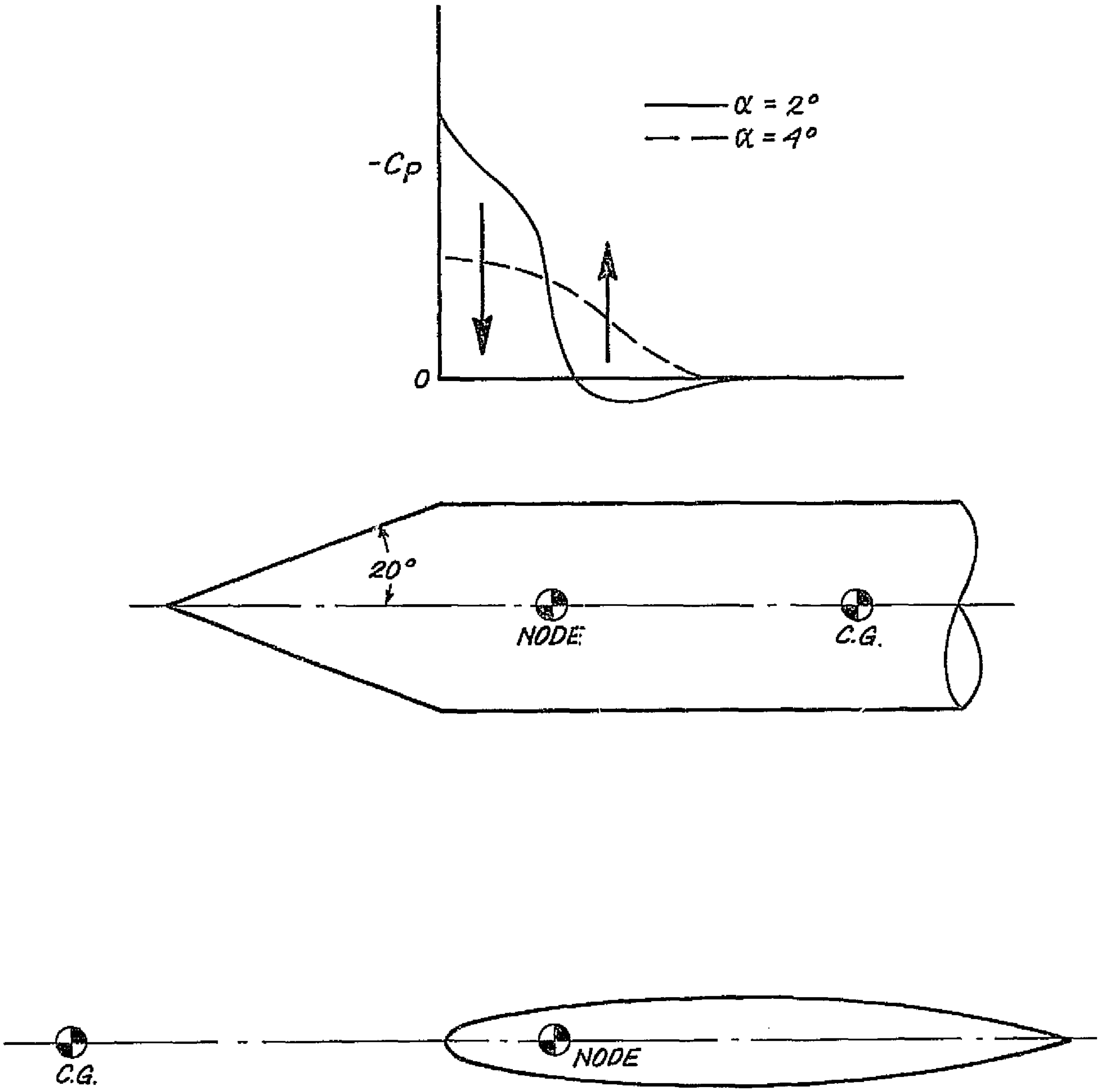

Figure 27 Sketch of Similar Shock-Induced Force-Couples on Cone-Cylinders and Airfoils

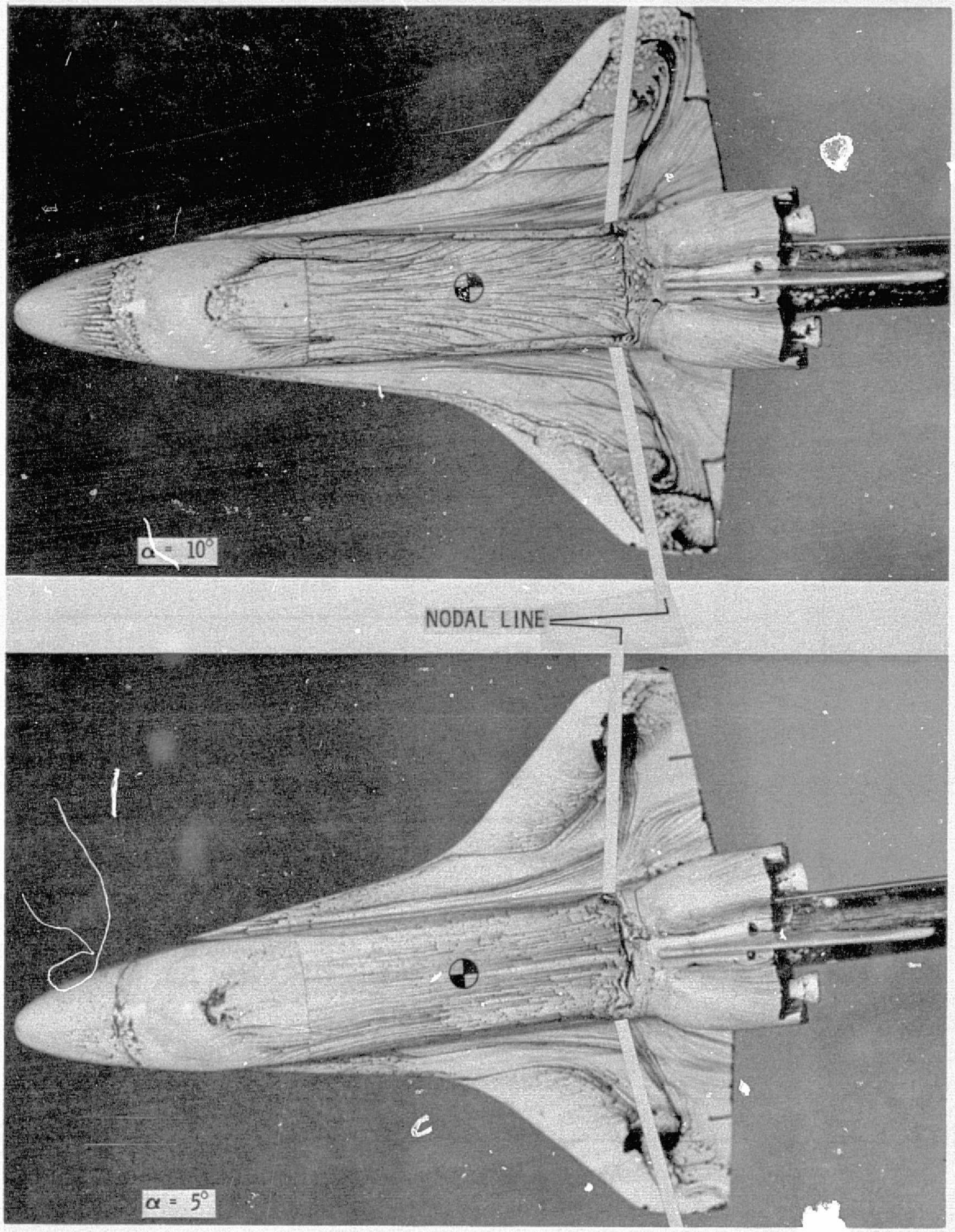

Figure 28 Flow Visualization Pictures of the Orbiter Wing at $\alpha = 5°$ and $\alpha = 10°$

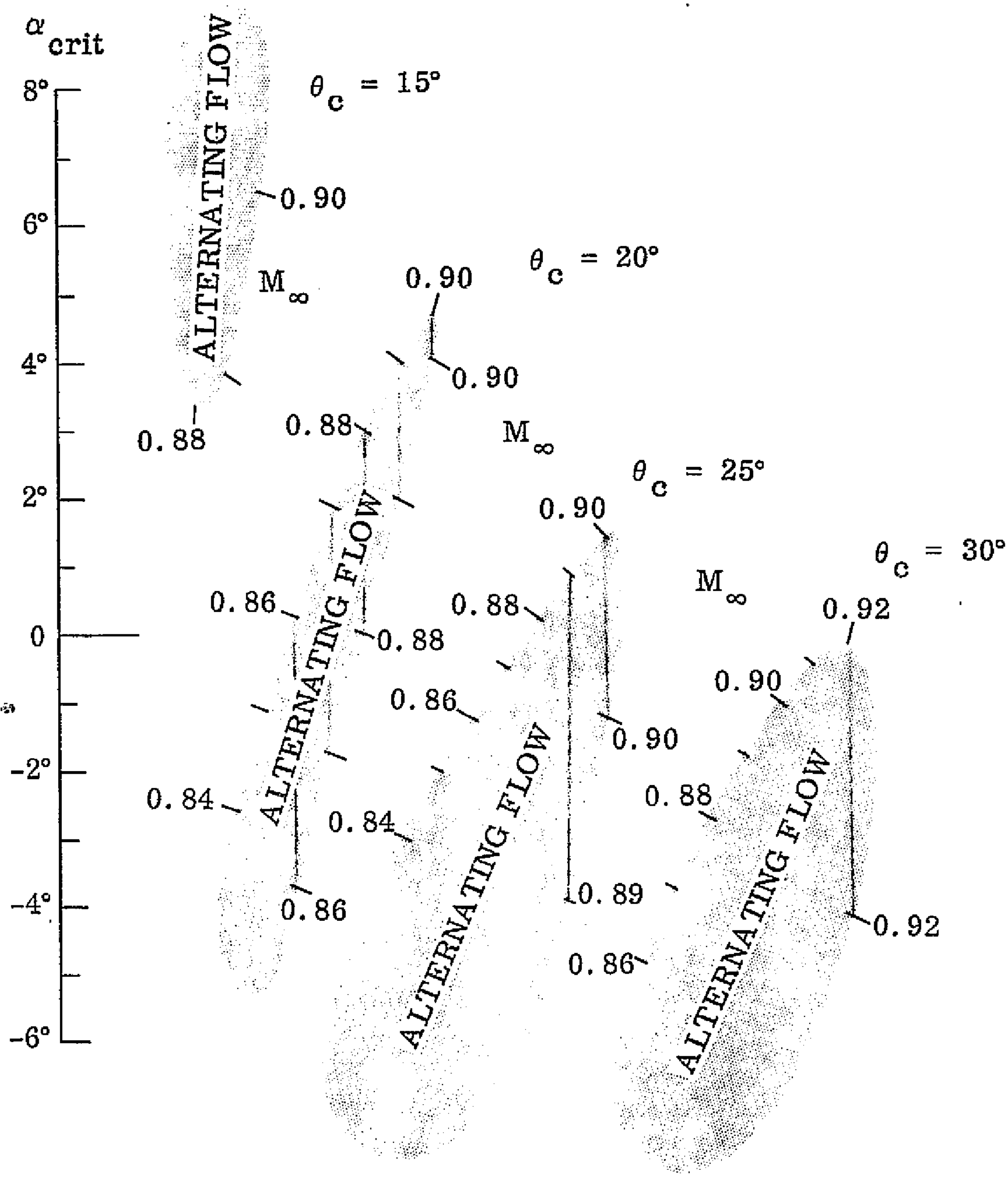

Figure 29 Critical Angle-of-Attack Regions for Cone-Cylinder Bodies

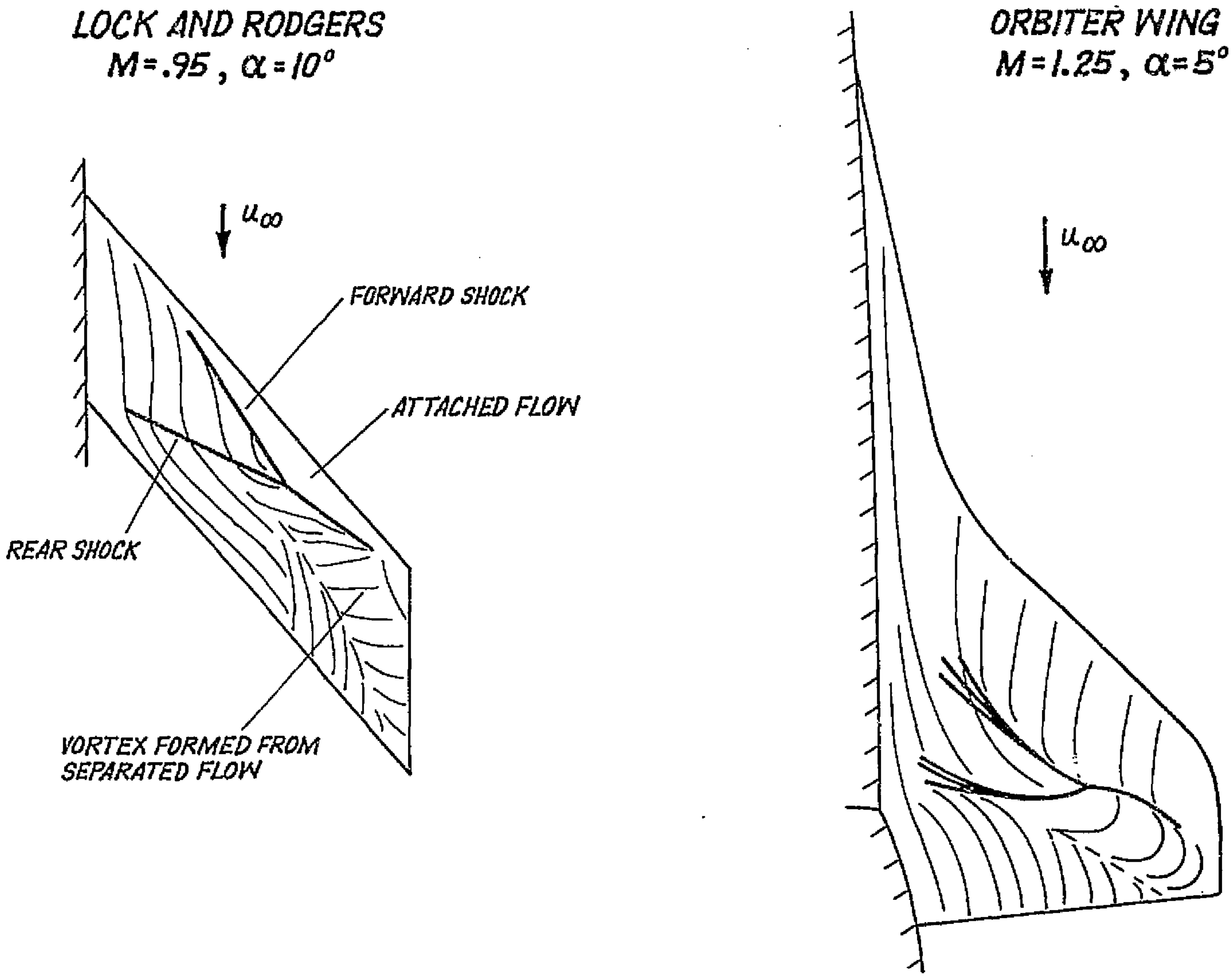

Figure 30 Wing Sweep Effect on Shock-Induced Flow Separation

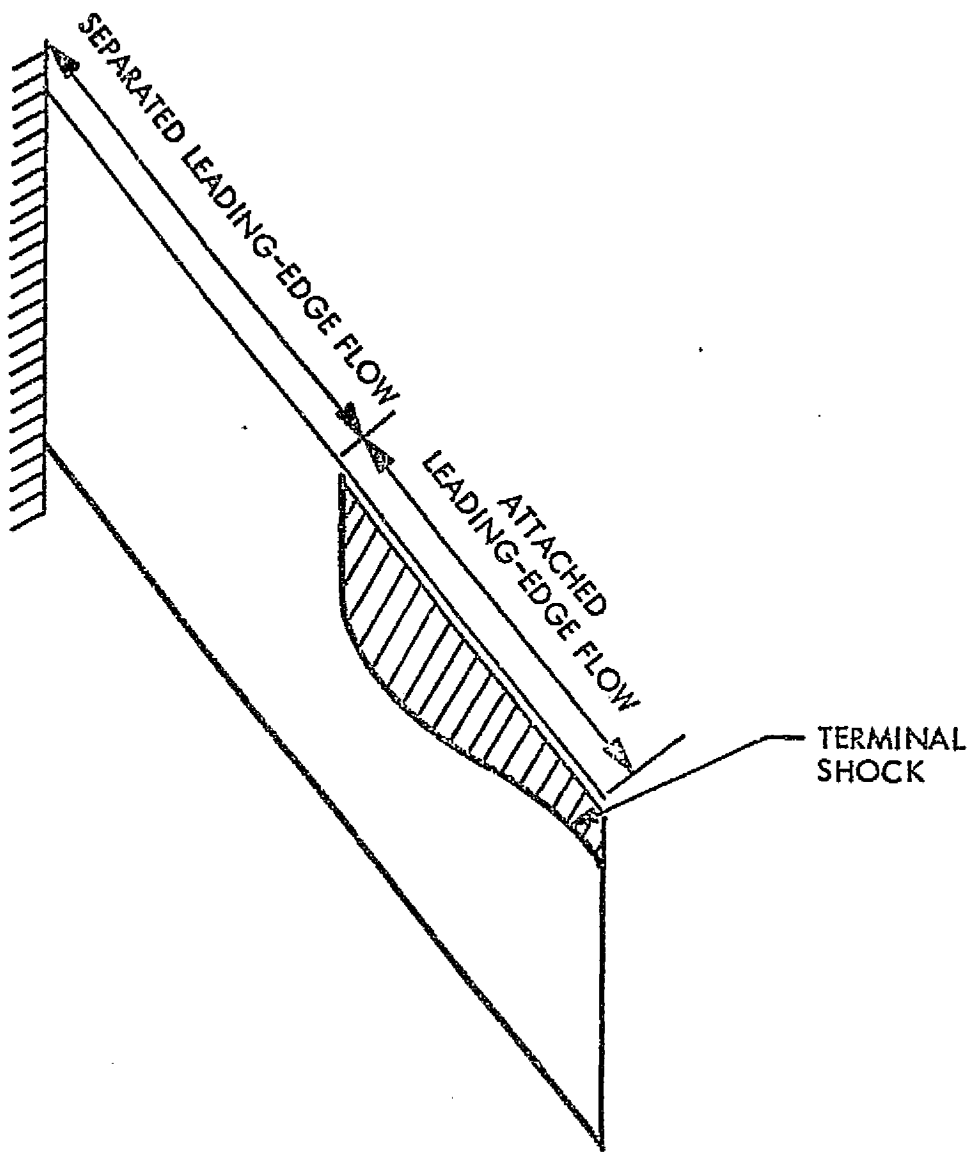

Figure 31 Effect of Early Transition of Spanwise Flow on the Shock-Induced Separation on a Swept Wing at $M_{\infty} = 1.05$, $\alpha = 6.6°$

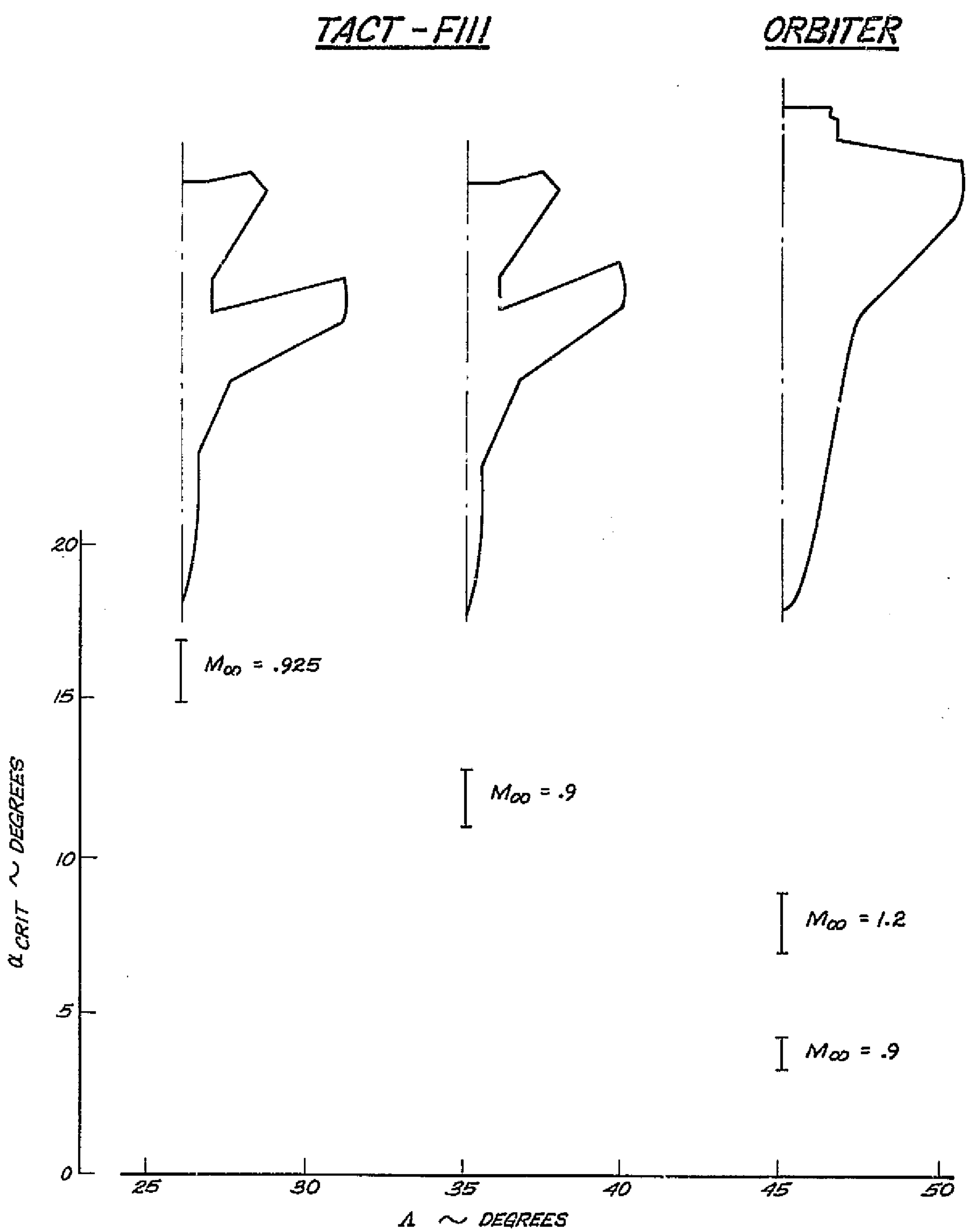

Figure 32 Effect of Leading Edge Sweep on Sudden Change of Shock-Induced Separation

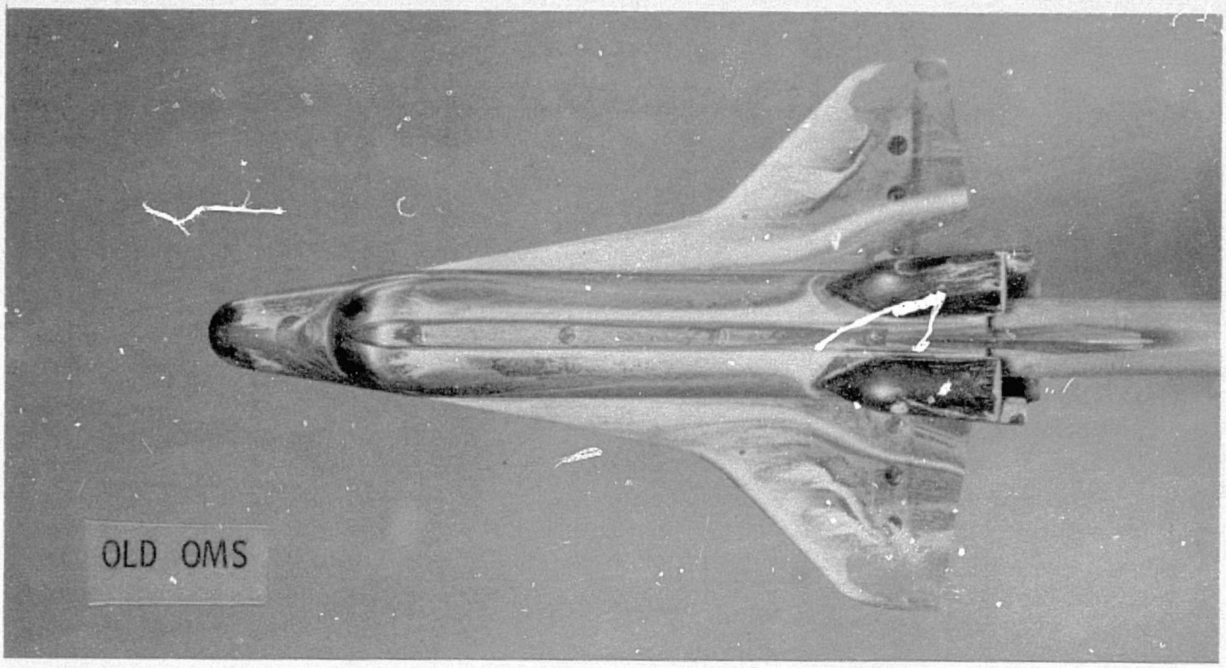

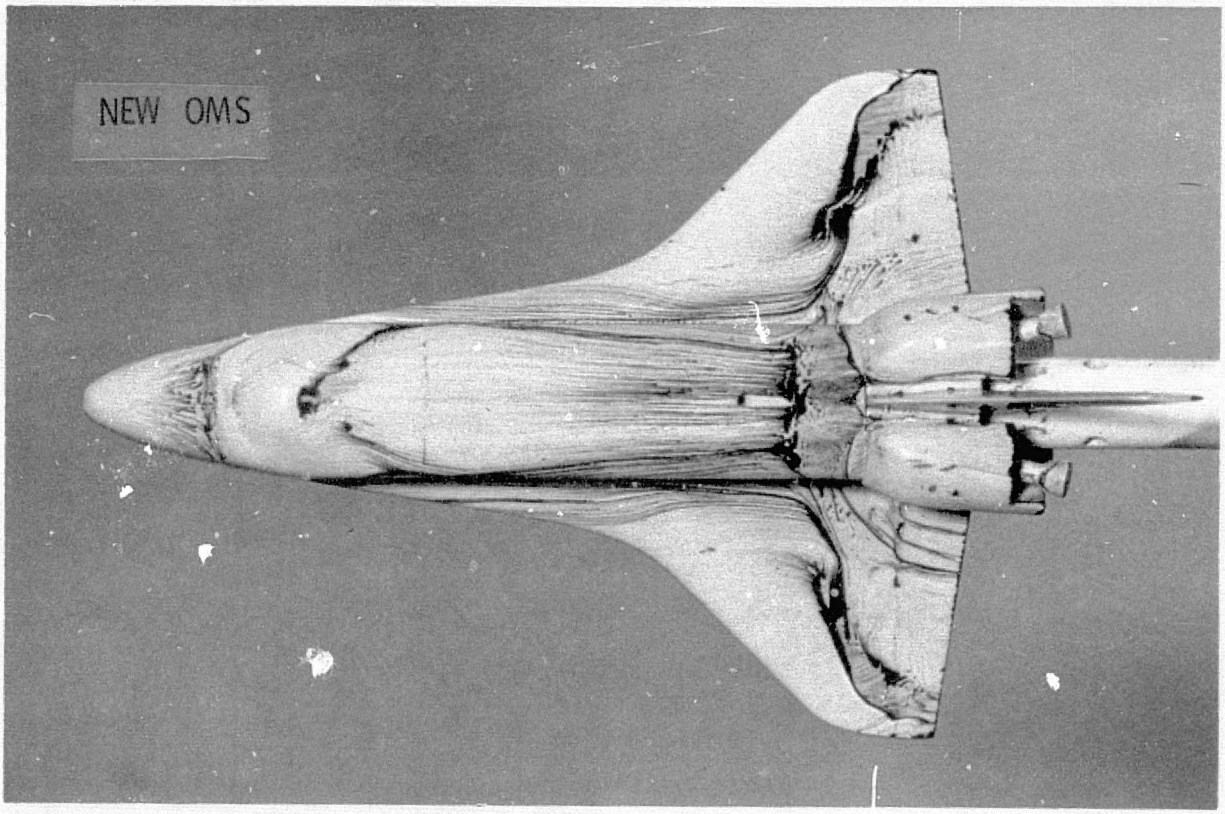

Figure 33 Effect of OMS-Pod Geometry on Orbiter Wing Flow at $M_\infty = 1.2$, $\alpha = 0$

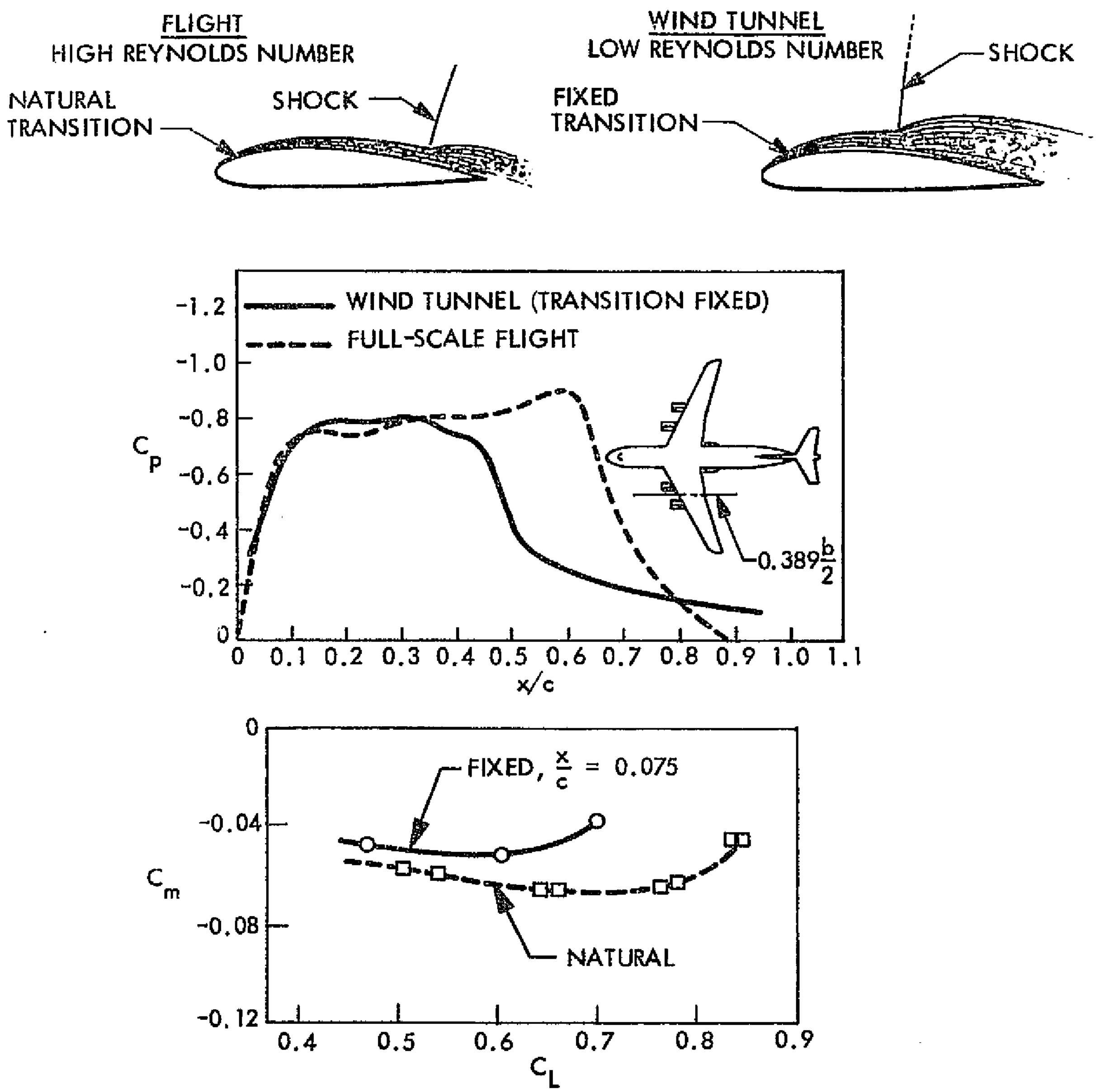

Figure 34 Scale Effects on Shock-Boundary Layer Interaction at $M_\infty = 0.85$